Valentin Vogl BSc

CFD simulation of a methane steam reformer for the steam-iron process

MASTER'S THESIS

to achieve the university degree of

Diplom-Ingenieur

Chemical and Process Engineering

submitted to

Graz University of Technology

Supervisor

Assoc.Prof. Dipl.-Ing. Dr.techn. Viktor Hacker
Institute of Chemical Engineering and Environmental Technology

Graz, December 2016

AFFIDAVIT

I declare that I have authored this thesis independently, that I have not used other than the declared sources/resources, and that I have explicitly indicated all material which has been quoted either literally or by content from the sources used. The text document uploaded to TUGRAZonline is identical to the present master's thesis.

Date

Signature

Acknowledgement

I would like to express my gratitude to my parents, who always supported me throughout my studies. Additionally, I also want to thank Viktor Hacker, Stephan Nestl, Sebastian Bock, Gernot Voitic and Robert Zacharias for their contributions to this thesis as well as the whole fuel cell systems group for an inspiring and dynamic working atmoshphere.

Abstract

Among the different pathways for the production of hydrogen, which is expected to fuel tomorrow's sustainable society, the Reformer Steam Iron Cycle (RESC) is a promising contender in the field of decentralised hydrogen generation. As the available space in the compact tubular reactor is limited, shortcomings in heat supply can occur and cause coking on the reforming catalyst, leading to reactor blocking and reducing feedstock conversion. The aim of this work is to ascertain the temperature profile in the reactor in order to predict the occurence of regions which tend to equilibrium carbon formation. To that end, a computational fluid dynamics (CFD) study was performed, the model scaled up and the process investigated for a representative operation point in a reactor of an industrial-scale diameter. Besides the development of a strong, customisable modelling tool for the methane steam reforming process, two main findings were made: Firstly, a region of low temperature with a minimum value of 404 °C was detected and the temperature distribution inside the reactor was documented. Secondly, it was found that the developed model over-estimates practical reaction rates of the main reforming reactions and subsequently over-predicts the temperature drop. Thus, it is concluded that large parts of the reactor show a propensity for equilibrium carbon formation. However, the developed reaction rate model must be adapted to the performance of an actual catalyst in order to be able to represent real experiments instead of ideal reaction behaviour. As no data for the modelled catalyst is yet available, the next step of model development must be the characterisation of the catalyst performance. All things considered, the conducted studies have yielded a mathematical model, which can be used for quick and thorough evaluations of heat and mass transport in the course of a RESC design process. This work provides new insights to the reforming section of the process, which led to the construction of a bench-scale reactor and facilitates the commercialisation of RESC technology.

Kurzfassung

Unter den vielen Prozessen zur Herstellung von Wasserstoff aus erneuerbaren Ressourcen stellt der Reformer-Eisen-Dampf-Prozess (RESC) eine vielversprechende Möglichkeit für die dezentrale Versorgung mit hochreinem Wasserstoff dar. Durch die begrenzte Größe des Reformers im kompakten RESC-System kommt der Wärmeeinbringung in den Reaktor besondere Bedeutung zu, um die Bildung von Kohlenstoffablagerungen am Katalysator bei zu niedriger Betriebstemperatur zu verhindern. Diese Arbeit zielt darauf ab das Temperaturprofil im Reaktor zu beschreiben, um eine Aussage über die Wahrscheinlichkeit von lokaler Kohlenstoffbildung unter Verwendung der Reaktionsgleichgewichte zu treffen. Hierfür wurde ein numerisches Strömungsmodell (computational fluid dynamics (CFD) model) entworfen und für einen praktisch relevanten Betriebspunkt ausgewertet. Neben der Entwicklung eines leistungsstarken, modular aufgebauten Simulationswerkzeugs zur Untersuchung der Methan-Dampfreformierung wurden zwei wesentliche Beobachtungen bei der Auswertung des Modells dokumentiert. Am Anfang des Katalysatorbetts beginnt eine Niedrigtemperaturzone mit einer mimimalen Temperatur von 404 °C, welche sich über weite Teile des Reaktors erstreckt. Der Vergleich von Simulationsergebnissen mit experimentellen Daten ergab, dass das Modell ideale Reaktionsraten berechnet, welche durch Katalysatoren in der Praxis aufgrund von kinetischen Limitierungen nicht erzielt werden können und somit in weiterer Folge zu einem großen Temperaturunterschied am Katalysatorbetteingang führen. Basierend auf diesen Ergebnissen neigen große Teile des Reaktors zu Kohlenstoffbildung aufgrund der Reaktionsgleichgewichte. Um eine präzisere Aussage über die tatsächliche Temperaturdifferenz treffen zu können, ist es nötig das Reaktionsmodell zu parametrieren. Da noch keine Daten des modellierten Katalysators verfügbar sind, muss das verwendete Material charakterisiert werden, um die idealen Reaktionsraten im Modell den realen anzugleichen. Es wurden im Zuge dieser Arbeit neue Erkenntnisse über den Reformierungsteil des Prozesses gewonnen, welche zum Bau eines Pilotreaktors führten und die zukünftige Kommerzialisierung des RESC-Prozesses vorantreiben werden.

Contents

1. Introduction

The expected impacts of climate change to environment and humankind call for extensive research of technologies to be able to curb these effects. The emission of greenhouse gases into the atmosphere entails phenomena that can already be witnessed, such as higher average temperatures and more extreme weather events [1]. In addition, extraordinary climatic situations must be reckoned with if the current global trend of increasing greenhouse gas emissions is upheld [2]. Therefore, in 2015 the United Nations Framework Convention on Climate Change approved a resolution to limit the effects of climate change by pursuing the goal of keeping the average global warming since pre-industrial times below 2°C [2]. Among the various strategies laid out in pursuit of this goal, enhanced energy savings and increased recycling for instance, one of the keystones of the project is replacing fossil fuels with renewable energy sources. During combustion of fossil fuels, greenhouse gases, such as CO, CO_2 and CH_4, are emitted into the atmosphere. The concentration of these compounds in the atmosphere influences its radiative balance and thus contributes to global warming [3]. The substitution of energy sources of fossil origin with renewable fuels could lead to a reduced amount of emitted greenhouse gases and consequently could decelerate global warming. The potential is great, as globally energy consumption from fuel still relies on fossil energy carriers (see figure 1.1).

While the list of possible sustainable fuels is long, non-fossil hydrogen is a promising contender [1]. The construction of a hydrogen economy, where most of the energy is supplied by conversion of hydrogen, has received wide attention not only from scientists, but also from politicians and companies [1]. Nowadays, hydrogen is mostly used as a bulk substance in the chemical industry and further processed into other products. However, its main intended purpose in a hydrogen economy will be the utilisation as fuel. The most compelling benefit of a world propelled by hydrogen is clearly the environmental compatibility of hydrogen conversion. The sole product from hydrogen combustion or electrochemical conversion with oxygen is water, without the formation of greenhouse gases. Thus, global emissions could be reduced in a hydrogen economy. A shift towards hydrogen as a fuel would entail further positive effects, such as energy security and the reduction of pollutant emissions in megacities, thereby improving public health [1].

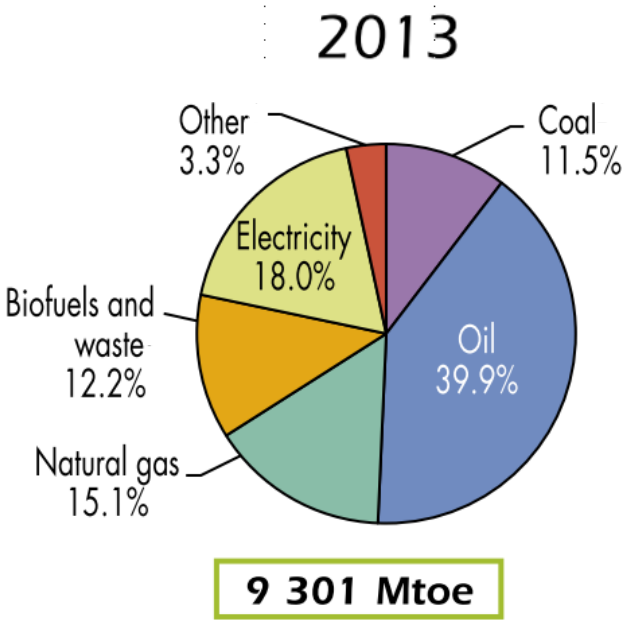

Figure 1.1.: 2013 World Energy Outlook: global fuel shares of total energy consumption [4].

Despite hydrogen being the must abundant element in the universe, it does not occur in its elemental form naturally and must thus be converted from other energy carriers. While today hydrogen is mainly produced from fossil-based feedstocks, it can also be obtained by converting biomass or via electrolysis. Therefore, in order to produce clean hydrogen, the production cycle has to be be carbon-neutral itself. In the transition phase from fossil fuels to renewable hydrogen, natural gas will play a significant role in promoting hydrogen technologies [1]. Despite its status as the cleanest fossil fuel, it is essential that the use of natural gas must also be phased out eventually and substituted by hydrogen.

Lately, interest in hydrogen has been increasing due to the advances in fuel cell technology [1]. In the transportation sector, the substitution of the gasoline-fuelled combustion engine with the hydrogen-driven fuel cell has great emission-saving potential. Worldwide, transportation accounts for 27.5% of the total energy consumption and is deeply reliant on fossil fuels (95% of fuel used for transportation is petroleum-based) [1, 4]. Hydrogen-based transportation could therefore have a strong positive impact on the global carbon dioxide balance. However, the main obstacle for the implementation of a hydrogen economy is the missing infrastructure for hydrogen transportation. In order to distribute the fuel effectively, a network of pipelines and filling stations must be created, requiring large investment efforts.

A determining factor in the realisation of this project is the willingness of governments to favour investments in hydrogen technology over the current fossil fuel-funding situation. Additionally, the successional adaption of mainstream energy policies and incentives in

order to promote a transition to hydrogen must be promoted [1]. Until the construction of such an infrastructure is realised, other ways of hydrogen supply at filling stations must be considered, for example by directly generating hydrogen on-site.

An auspicious option is the decentralised production of hydrogen with the Reformer Steam Iron Cycle (RESC) technology. By operating smaller, decentralised units, hydrogen can be produced independently of an available distribution network on-site. Additionally, feedstock flexibility of the operated process can provide the option of utilising locally available resources for hydrogen generation. In combination, these advantages yield promising solutions for rural regions by enabling hydrogen production in remote areas. The RESC process, which combines a steam reforming section and a steam-iron process unit, unites both these advantages. The feedstock is supplied to a catalyst-filled reformer and converted to synthetis gas, before it is led through a iron-oxide porous bed, reducing the oxide to iron (see figure 1.2). Both operations take place in one tubular reactor in serial configuration, hence ensuring a simple reactor design. In a consecutive process step, pure water steam is fed to the iron oxygen carrier in counterflow direction, oxidising the iron and converting water to pure hydrogen ($>$ 99.95%) [5].

The steam-iron process is a well-known technology for hydrogen generation [6]. The combination of steam reforming and steam-iron process, referred to as RESC, was developed and studied extensively at the Institute of Chemical Engineering and Environmental Technology at Graz University of Technology. Hacker *et al.* investigated the conversion of biomass and gasified coal in a steam-iron application for a fuel cell purpose [7, 8]. Later, a reforming section was integrated into the system and thus the foundation of the RESC process built [9]. Thermodynamic considerations of both reforming and steam-iron reactions were conducted by Fraser in the past [10]. Experiments in fixed-bed reactors containing both reforming and steam-iron section were later performed by Nestl, which are used as a basis for the investigations discussed in the present work [5, 11].

In this work, steam reforming of methane in the reforming section of a RESC reactor with an industrial-scale diameter is investigated. Natural gas was used as feedstock and a conversion to syngas for a further use for hydrogen generation was simulated. In order to evaluate the performance of the reformer section, a computational fluid dynamics (CFD) model was developed and the equation system solved numerically. The model increases the process understanding at the operating point for the purpose of reactor design evaluations. In addition, equilibrium compositions at different process conditions were studied. The validation of the model with a prototype reactor was conducted and simulation results for an industrial-scale reactor are presented in this thesis. A validation cycle for the studied

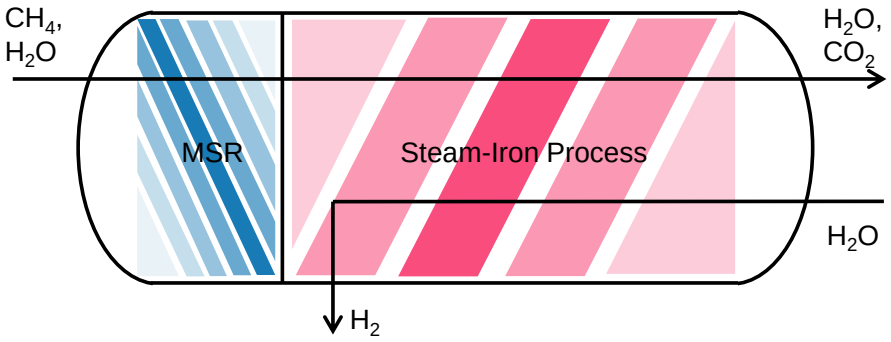

Figure 1.2.: Schematic illustration of a Reformer Steam Iron Cycle (RESC) reactor.

reactor must still be performed in the future, along with the further refinement measures suggested in the discussion chapter of this work. The main objectives of the investigation are the assessment of feedstock conversion and the temperature profile inside the reactor. Full conversion of methane is a desired result, as it directly increases the performance in the steam-iron section. If the temperature inside the fixed-bed reactor decreases too much, carbon formation can occur and lead to the reduction of catalyst activity and blocking of the reactor.

This work is divided into three main sections. Firstly, fundamental theoretical aspects are summarised in chapter 2, which are important for the interpretation of the results. In this section, the main points of RESC, methane steam reforming and CFD technology are addressed. Secondly, the structure of the CFD model is explained in chapter 3. This part is structured in the style of the model development process, starting with the definition of the system boundaries and the discretisation of the system. Then, the equations used to describe the process in the system are discussed, which contain mass, momentum and energy balances as well as chemical reactions. In conjunction with the system of equations, assumptions and simplifications are addressed and the set of boundary conditions is laid down. In the final part of the model development section, information about the numerical solving process is provided. Finally, the system of equations was solved and the results are discussed in chapter 4. Special consideration is granted to the impact of the predicted reactor temperature and its probable consequences. A summary of the most essential insights and its implications for RESC research is provided at the end of the thesis.

2. Theory

Important theoretical aspects are presented in the following chapter, which are later referred to in the analysis of data obtained from the calculations. At the beginning, a description the working principle of the Reformer Steam Iron Cycle (RESC) is given and special attention is devoted to the reforming section of the system. In this context the basics of methane steam reforming (MSR) are discussed. Finally, before going into detail on the description of the model development process, the fundamental aspects of computational fluid dynamics (CFD) modelling, which are relevant for the presented studies, are addressed.

2.1. Reformer Steam Iron Cycle

Research activities investigating the steam iron process (SIR) have long tradition in the fuel cell group of Graz University of Technology Institute of Chemical Engineering and Environmental Technology. The developed sponge iron reaction (SIR) and its further advancement, the Reformer Steam Iron Cycle (RESC), are based on a process that was already used in the early 20^{th} century [6]. Due to the increasing demand for hydrogen from renewable energy sources, the SIR was rediscovered as a promising way to generate low cost hydrogen with comparably high efficiency [7]. A chemical looping principle is applied in order to produce highly pure, high-pressure hydrogen. Due to its purity, it can be directly utilised in any kind of fuel cell without the necessity of typical production post-treatment processes such as CO_2 removal, PSA or other purifiers [8, 9].

The SIR utilises two consecutive reactions to generate pure hydrogen from the used feedstock. As the same reactor is used for both steps, the operations are conducted in batch mode. First the feed is brought into a tubular reactor, which is filled with a porous metal oxygen carrier, typically iron-based. A reduction of the iron oxide takes place and Fe_2O_3 (hematite) is reduced to Fe_3O_4 (magnetite) and further to FeO (wuestite) and Fe. The lean gas, which leaves the reactor, contains a mixture of water, carbon dioxide, carbon

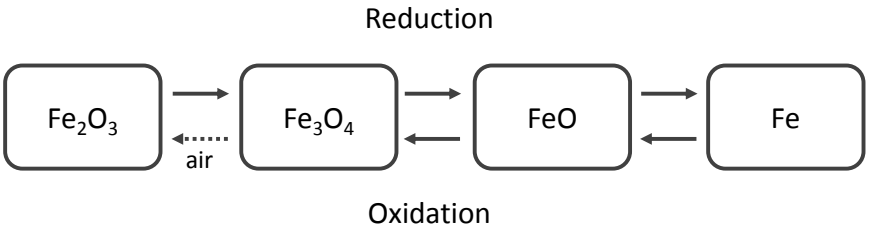

Figure 2.1.: Schematic illustration of the different iron states during the reduction and oxidation phases in the steam-iron process. The dotted arrow represents the regeneration of the oxygen carrier with air or pure oxygen.

monoxide and hydrogen with a composition that depends on the reduction step that has been reached in the reactor. In the second step, the reactor, now filled with pure Fe, is fed with hot steam, which oxidises the iron back to Fe_3O_4 via the same path it was reduced before. However, the oxidation to Fe_2O_3 with steam is not possible, whereas the oxygen carrier can be regenerated from Fe_3O_4 to Fe_2O_3 with oxygen or air if this is demanded. If not, the SIR process can be performed between the Fe_3O_4 and the Fe state. The result is pure hydrogen, which is then withdrawn from the reactor as the final product. The reaction paths for reduction and oxidation are described in figure 2.1 and the respective reactions presented in equations (2.1) - (2.4) [5]. The cyclic nature of the process can be used in respect to the current on-site hydrogen demand. If no more fuel is needed, oxidation can be delayed and the oxygen carrier left in its Fe state. When fuel demand increases, the oxidation process can then be executed again. Hydrogen can thus be stored without typical losses, such as boil-off [11].

$$total: \quad Fe_2O_3 + 3H_2 \rightarrow 2Fe + 3H_2O \tag{2.1}$$

$$3Fe_2O_3 + H_2 \rightarrow 2Fe_3O_4 + H_2O \tag{2.2}$$

$$Fe_3O_4 + H_2 \rightarrow 3FeO + H_2O \tag{2.3}$$

$$FeO + H_2 \rightarrow Fe + H_2O \tag{2.4}$$

$$2Fe_3O_4 + \frac{1}{2}O_2 \rightarrow 3Fe_2O_3 \tag{2.5}$$

During the reduction, iron oxide is reduced to pure iron in the presence of hydrogen or carbon monoxide. Therefore, the described H_2 in the equations can be replaced by CO, which also has the potential to reduce the oxide. During the oxidation process reactions (2.3) - (2.4) are reversed. However, only a reaction to magnetite is possible, which is why it is more useful to operate the process between the Fe_3O_4 and Fe state. It is then possible to regenerate the oxygen carrier to hematite with air, following reaction (2.5). Besides being able to resume the original state, remaining carbon depositions on the oxygen carrier can also be removed this way.

Over the past few years, great progress has been made in the development of processes based on the sponge iron reaction. Several different fuels (biomass, coal, syngas, liquid hydrocarbons) were investigated under SIR process conditions [7–9]. These experiments suggest that the process is very versatile and can be adapted for different fuel requirements. One example is the combination of SIR process and solid oxide fuel cell (SOFC), which has been demonstrated successfully [8]. Current studies concentrate on improving the performance of the oxygen carrier.

Recent studies have addressed the influences of operating pressure on the performance of the process [11]. When the oxidation is performed at elevated pressure the product gas can thus be directly stored in high pressure vessels. During the reduction, however, elevated pressure must be avoided. This is due to a decrease of CH_4 conversion in the reforming section at high pressure, which requires a high steam-to-carbon ratio (S/C) for acceptable conversion rates. Subsequently, this alters the composition of the produced synthetis gas by adding more water and lowering the share of reducing agents.

There are multiple reasons advocating the inclusion of a steam reformer. Firstly, the overall efficiency of the process can be increased, when a higher caloric gas is fed to the reactor [9]. Secondly, the direct conversion of methane or higher hydrocarbons can be incomplete, leading to considerable amounts of unreacted methane in the lean gas. This is due to the nature of the methane conversion reaction, which is strongly temperature dependant and slow [9, 10]. Finally, coking is a key problem in the operation of RESC reactors. Deposited carbon is partially removed by the steam in the oxidation step and can subsequently be found in the product as CO and CO_2. Recent studies have shown the necessity of a prior reforming step before the reduction process [11]. When methane enters the reduction section, carbon might be formed as described in reactions (2.6) - (2.7) [11].

$$CH_4 \rightarrow C_s + 2H_2 \tag{2.6}$$

$$CO + H_2 \rightarrow C_s + H_2O \tag{2.7}$$

$$C_s + xH_2O \rightarrow CO_x + xH_2 \tag{2.8}$$

Full inhibition of carbon deposition is difficult, as the iron was reported to catalyse coke formation [11]. Carbon was mainly found close to the inlet and at the end of the reactor [5, 11]. This was reasoned to be because of a lower reaction temperature, caused by insufficient heating and the highly endothermal behaviour of the methane steam reaction [11]. During the oxidation process, some of the formed carbon can be removed again by reacting with the supplied water to form CO or CO_2 according to reaction (2.8). If so, CO and CO_2 can be found in the effluent and thus decrease the product gas quality. This is especially undesirable when a further use of the produced hydrogen in low-temperature fuel cells is planned, which are sensitive to CO and CO_2. However, part of the deposited carbon also remains in the reactor and therefore accumulates with every process cycle.

As a result of its simplicity compared to other hydrogen production technologies, the RESC-process can be regarded as a competitive alternative for the decentralised generation of hydrogen, at filling stations for instance. As mentioned above, RESC technology replaces additional process steps, such as shift conversion, CO_2-removal, molecular sieves, purifiers, PSA and liquid nitrogen scrubbing, as purified hydrogen can directly be withdrawn from the process [9]. In short, it can be said that the RESC process unifies production, purification and storage of hydrogen in one process [11]. Additional simplification of reactor design is enabled by the nature of the reforming and reduction processes. Both are promoted by low pressure and a high temperature above 800 °C, which makes it possible to interconnect them without the need for compressors, valves or heat exchangers between the sections. The idea of designing a reactor containing all process steps originates from these benefits and shall be further addressed later on in this work.

Mathematical modelling studies of the RESC process were reported in the past [10]. Basic assumptions included isothermal reforming conditions and ideal thermodynamic behaviour. Chemical equilibria were investigated by Gibbs energy minimisation calculations [11]. As the temperature varies strongly and thus the assumption of an isothermal reactor is not ac-

ceptable for reactors of large diameters, further investigation of the temperature distribution inside the catalyst bed is motivated. The calculation of chemical equilibria for the present process will be addressed in section 4.1.

2.2. Methane Steam Reforming

Methane steam reforming (MSR) is an important process for the production of synthesis gas, a mixture of hydrogen and carbon monoxide and important feedstock for the methanol industry. It is an industrially mature process and used on a big scale, for instance for the synthesis of ammonia or the production of H_2 as a fuel for fuel cells as well as combustion engines [12]. Usually, the feedstock is supplied to an array of catalyst-filled tubular reactors, which are embedded in a furnace [13]. MSR is commonly performed with natural gas, however, higher hydrocarbons are also converted to hydrogen industrially. Several pre- and post-treatment operations have to be performed depending on the type of the feed in order to obtain high-quality syngas or hydrogen as a product. Pre-treatment operations include heaters, the addition of product hydrogen to the feed, hydrotreaters to split up higher hydrocarbons and convert higher sulphur molecules to H_2S and a consecutive zinc-oxide bed for the removal of the H_2S fraction. Post-treatment operations provide heat recovery, further conversion in a shift converter and purification of the product, including water removal in a separation drum and pressure-swing adsorption (PSA), if pure hydrogen is the product of choice [14]. Industrial-scale reforming plants have up to several hundred tubular reactors with lengths of over 10 m each and a typical tube diameter of 120 mm [14]. In the furnace, heat is supplied to the reactors by burning fuel, which leads to furnace gas temperatures above 1100 °C. The reforming process is conducted at temperatures above 800 °C, with variations from reactor inlet to outlet from 600 °C to 870 °C. MSR plants are designed for average lifetimes of 100,000 hours and capacities from 100 to 140,000 $Nm^3 \cdot h^{-1}$ [12, 15].

Several important physical principles determine the performance in the catalyst-filled tubular reactors, in which the reforming process is performed, as schematically illustrated in figure 2.2. Due to the partially particle-blocked cross section, a complicated velocity profile develops and a pressure drop along the reactor centreline can be observed. In tubes with small tube to particle diameter ratios, the velocity reaches its maximum in the vicinity of the wall, whereas this effect is subsequently mitigated when this ratio increases [16]. For high ratios, plug flow can be a valid assumption for simulation purposes [16]. On the particle surface, three major reforming reactions as well as side reactions are catalysed. The reforming reactions show an overall endothermic behaviour, which requires the supply of heat to the reactor. As

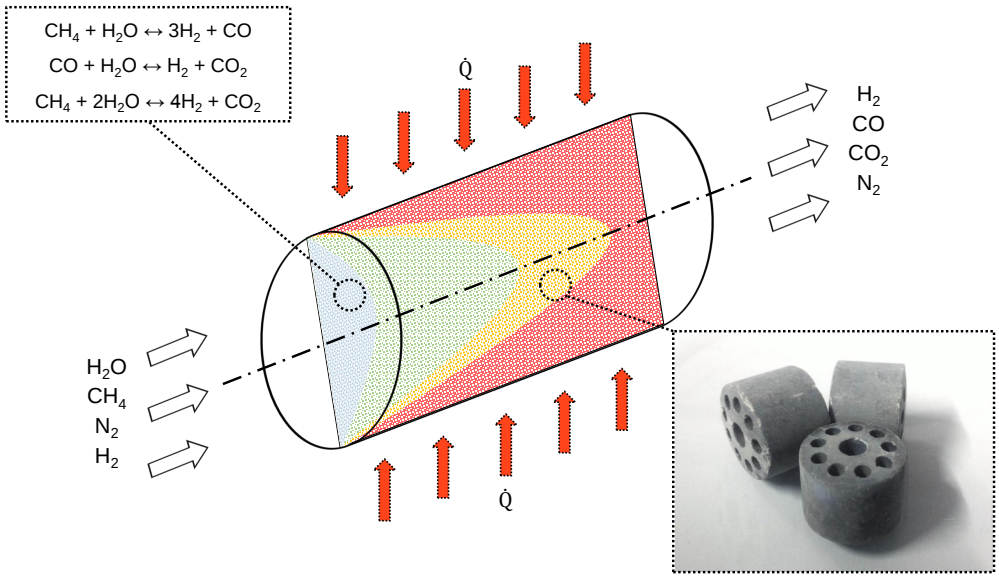

Figure 2.2.: Schematic illustration of the methane steam reforming process in a tubular reactor. Typically a temperature profile develops as the catalyst bed cools down due to the onset of endothermic reforming reactions. The cylindrical catalyst pellet depicted is an example, however, the modelled particle has no holes.

the preservation of the operating temperature is desired, effective heat transport towards low-temperature regions is important to the MSR process. The significance of heat transfer relates to the fact that low-temperature sections are prone to undesired carbon formation, which can have negative effects on the process, such as a reduction of efficiency and catalyst breakdown as described in section 2.2.2. Careful consideration of the heat flux distribution is a major task for the system designer in order to avoid hot spots or hot bands and subsequent coking [13]. Important parameters to ensure the safe and successful operation of a MSR reactor are the steam-to-carbon ratio S/C, feed and tube wall temperatures, the pressure drop and the feed flow rate. Additionally, catalyst material and structure, tube length and diameter play a significant role in the performance of the process.

Besides careful reactor design, a successful reforming process requires the choice of suitable operating conditions and high performance of the catalyst. Typical inlet temperatures range from 450 °C – 650 °C, while the synthesis gas leaves the reactor at 700 °C – 950 °C. In the furnace, only about 50% of the produced heat can be directly utilised by the reactors. The rest is recovered from flue gas and used for pre-heating of the reformer feed. Thus, thermal efficiencies of 95% can be achieved [12]. Requirements for a successful operation of the process are full conversion of the feedstock, a constant pressure drop in order to provide uniform flow conditions and a sufficiently low wall temperature to ensure a long life of the reactor tubes [13]. The catalyst must provide high activity, mechanical strength and a resistance to carbon formation. Common challenges during the operation are high

thermal stresses in tube walls, carbon deposition as well as sulphur poisoning of the catalyst. The reactor walls must endure big stresses due to high wall temperatures and heat fluxes. Moreover, a non-uniform catalyst loading can lead to local overheating and therefore reduce the life of the tube [13]. Hot spots or bands might also be caused by carbon deposition on the catalyst and subsequent blocking of the reactor voids. Finally, the feedstock must be purified from sulphur prior to the reforming process step. Sulphur compounds are typically present as H_2S, thiols or COS and block the active sites of the catalyst [15]. The most established commercial catalyst Ni is especially prone to sulphur poisoning, while noble metal catalysts have a higher resistance, but are often not economically viable options.

During the reforming process, which is also referred to as Oxygenolysis in literature, three main reactions take place in the reactor [13, 15, 17]: reaction (2.9) to CO and H_2, which is also known as reverse Fischer-Tropsch synthesis, the water-gas shift reaction (WGSR, reaction 2.10)) and reaction (2.11) to CO_2 and H_2. It is obvious that reaction (2.11) represents the addition of the former two reactions, thus the reaction enthalpy equals the sum of other enthalpies and the equilibrium constant the product of the constants of the subreactions. Nevertheless it is worth noting that CO an CO_2 are both primary reaction products, so both reforming reactions actually take place simultaneously [18]. As a result methane can be converted in two different ways, either to carbon monoxide or carbon dioxide. Which reaction is favoured depends on the local temperature and the steam-to-carbon ratio S/C of the feed. If S/C is below 2 not enough water is present in order to convert all methane to CO_2. Overall, the relative kinetics of the two reforming reactions at local process conditions determine which reaction is dominant.

$$CH_4 + H_2O_{(g)} \rightarrow 3H_2 + CO \qquad \Delta H_R = +205\,\mathrm{kJ \cdot mol^{-1}} \qquad (2.9)$$

$$CO + H_2O_{(g)} \rightarrow H_2 + CO_2 \qquad \Delta H_R = -41\,\mathrm{kJ \cdot mol^{-1}} \qquad (2.10)$$

$$CH_4 + 2H_2O_{(g)} \rightarrow 4H_2 + CO_2 \qquad \Delta H_R = +164\,\mathrm{kJ \cdot mol^{-1}} \qquad (2.11)$$

It can be seen that the reforming reactions lead to an increase of moles and therefore also volume increase. By applying the principle of Le Chatelier it can be reasoned, that high operating pressure would shift the equilibrium away from the product side, which is why ambient operating pressure is adapted in order to promote conversion.

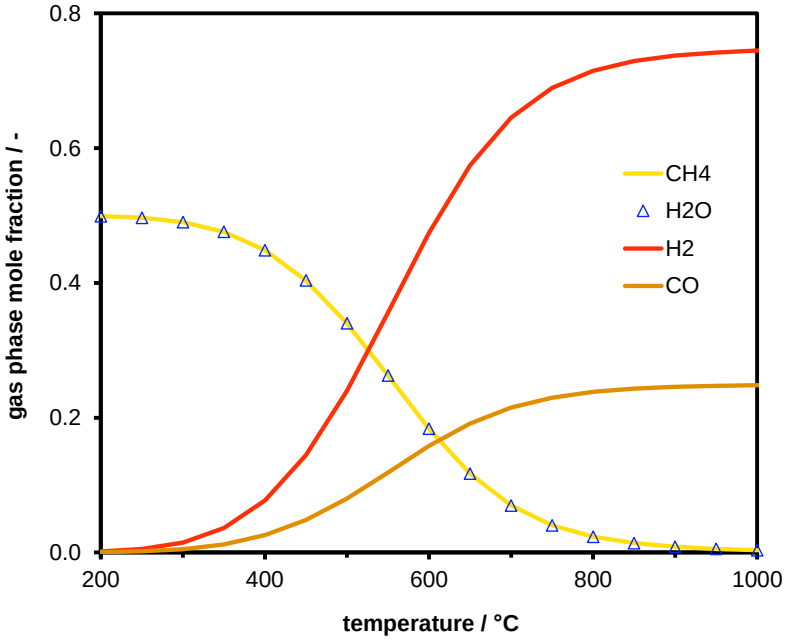

Figure 2.3.: Methane steam reforming to carbon monoxide, equilibrium as a function of temperature, S/C = 1.

In industrial reforming plants containing tubes with lengths of several meters, the outlet compositions usually are very close to equilibrium [15]. The reforming process can also be operated with carbon dioxide instead of water vapour, or both, to adjust the H_2/CO ratio of the synthesis gas for instance. Figures 2.3 - 2.5 show the temperature-dependent reaction equilibria of the three dominant process reactions. A look at the equilibrium compositions for the two reforming reactions indicates that high temperatures promote conversion of methane to hydrogen. While compositions show a high temperature dependency between 400 °C and 800 °C, the amount of hydrogen converges towards a steady value for higher temperatures. This suggests an operating temperature between 800 °C and 1000 °C, as a further elevation of the temperature has little effect, but increases the heating demand as well as thermal stresses in the reactor walls. The water-gas shift reaction equilibrium shows a slight preferation of CO over CO_2 in the suggested operating temperature interval. At 800 °C species fractions are equal with the formation of CO becoming more likely as the temperature increases. A comparison of methane conversion in the two reforming reactions shows that at a given temperature above 550 °C more CH_4 can be converted to CO than to CO_2. Having said this, the maximum hydrogen content of the product gas is higher in reaction (2.11), which can be explained by the comparison of the reaction equations. While the maximum hydrogen fraction of reactions (2.9) is 0.75, it can be 0.8 for reaction (2.11).

While trends and favourable operating conditions can be derived from equilibrium considerations, the activitiy and selectivity of the catalyst influences the composition notably. Therefore, an investigation of the used catalyst under realistic operating conditions must be

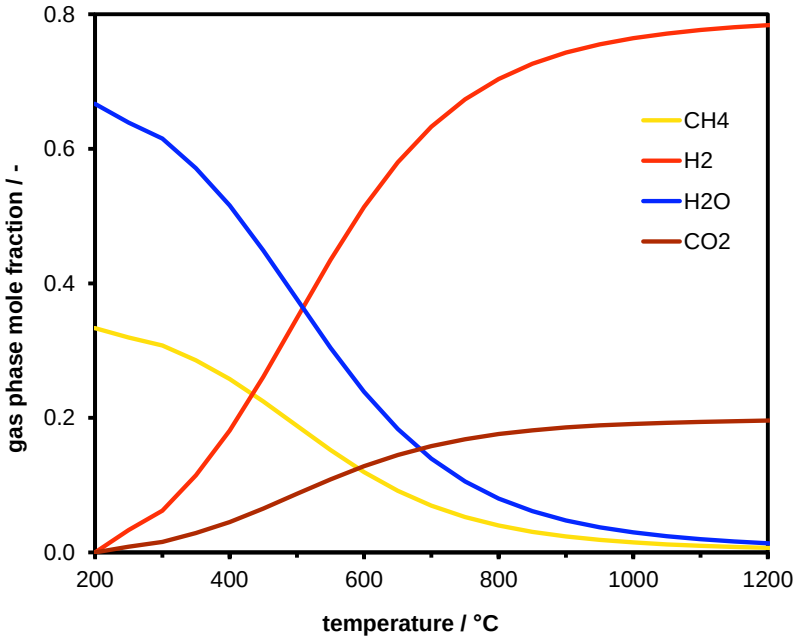

Figure 2.4.: Methane steam reforming to carbon dioxide, equilibrium as a function of temperature, S/C = 2.

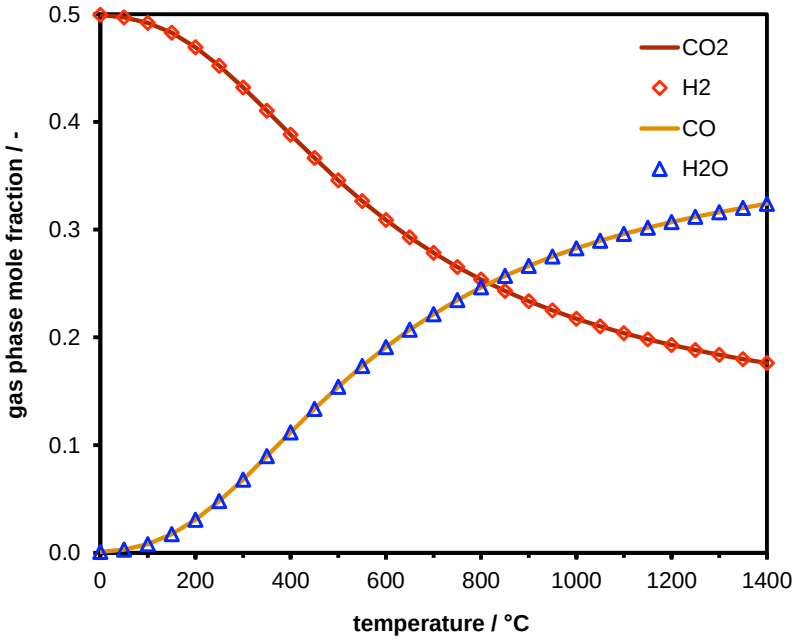

Figure 2.5.: Water-gas shift reaction equilibrium as a function of temperature, $CO/H_2O = 1$.

performed in order to assess the relative participation of the reforming reactions. Outside of the catalyst performance, the geometric structure of each particle and, furthermore, of the catalyst bed can have a significant influence on the reactions. The assessment of intraparticle mass transfer restrictions has high importance for the description of the process [19]. Kinetic studies reported severe mass diffusion restrictions, which are caused by pore diffusion into the catalyst bed [12]. These limitations of reaction kinetics are often considered in reaction models by using so-called effectiveness factors, which directly limit the reaction rate. Factors of 0.4 to below 0.1 were reported [12, 20]. For an accurate determination, pore diffusion in the used catalyst material has to be characterised first. In addition to mass flow restrictions, also the dominant mechanism of heat transfer inhibition was addressed [12]. While solid-solid conduction is regarded as a rapid mechanism, the gas film between particles is the main restriction for heat transfer in the reactor.

2.2.1. Thermal Management

Due to the endothermic reforming reactions, heat must continuously be supplied to the reactor by an external heat source. Effective heat distribution inside the reactor is a key requirement during the operation of a reformer. The energy balance of the reactor system is highly interdependent, because chemical reactions not only consume energy, but their equilibrium also changes with varying temperature. In addition, alterations of process temperature, as well as changes in local composition due to chemical reactions, modify physical properties such as density, viscosity and specific heat, which then retroact on the energy balance.

For tubes with industrial-scale diameters of 120 mm, effective radial heat transfer is a substantial feature in order to limit the temperature decrease near the inlet of the catalyst bed. As the highest reaction rates can be expected in the inlet section of the bed where the reactions start, the largest temperature drop is expected here. This is crucial, as regions of low temperature are prone to carbon deposition, which can have several negative effects on the process as it will be discussed in section 2.2.2. Due to the large diameter, heat transport towards the reactor centreline is slow. The dominating effect is thermal conduction, while the contribution of radiation depends on the maximum temperature of the heating device. The influence of radial enthalpy transport from the wall towards the reactor axis is an effective means for radial heat distribution, however the effect is small for random packings without the installment of deliberate flow redirections, as applied for instance in radially perfused monolith packings.

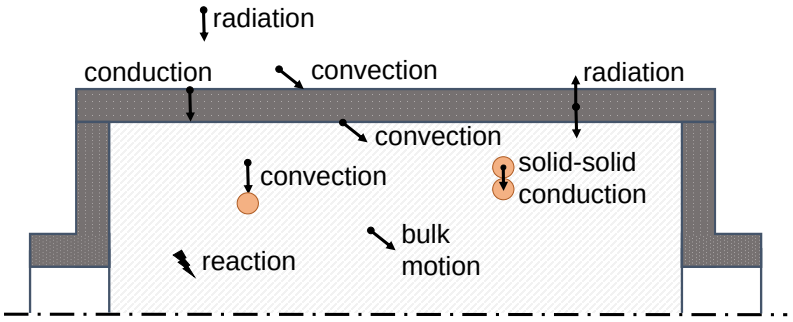

Figure 2.6.: Schematic illustration of the different heat transfer mechanisms, which have to be considered in the methane steam reformer (MSR) modelling process [14].

As previously explained, the temperature typically varies radially, especially in the entry section of the reactor. Towards the reactor outlet, the temperature profile becomes more uniform, as energy is conducted from the hot wall towards the colder centre, thus causing a non-constant axial temperature profile. In order to properly describe the heat distribution inside the catalyst bed, several heat transfer mechanisms have to be distinguished, which are illustrated in figure 2.6. The reactor wall is heated by radiation, thermal conduction and convection, if the fluid in the oven is in motion. While the wall conducts heat, it also emits thermal radiation. At the inner wall, the wall heats the fluid by means of convection. In the reactor, the occurence of chemical reactions influences the energy balance due to their reaction enthalpies. Fluid-particle heat transfer occurs by convection, while particle-particle heat transfer through conduction also has to be considered. Finally, enthalpy is transported in and out of the reactor through the motion of process gas in accordance with the local velocity profile. While all these effects must be addressed, their contributions to heat transport are of different magnitudes. For systems with high tube to particle diameter ratios in particular, as under investigation in this work, detailed consideration of the effects mitigating the radial temperature gradient is most important, with fluid-particle particle heat transfer also playing a role, especially when the bed porosity is low. Intraparticular heat transfer can often be neglected, when the temperature distribution inside the reactor is the target of examination [19].

2.2.2. Carbon Deposition

Carbon formation is a crucial problem in methane steam reforming, as it leads to catalyst breakdown and further blocking of the reactor, inhibits the catalyst and subsequently entails a decrease of feedstock conversion. When methane is used for reforming, coke deposition

either happens due to a shift in the Boudouard equilibrium (reaction (2.12)) or by direct decomposition of methane (reaction (2.13)) [21]. The contribution of a third reaction, in which carbon monoxide reacts with hydrogen to form solid carbon and water was also reported (reaction (2.14)) [17]. This reaction can also be utilised to regenerate the catalyst by gasifying carbon depositions with the supply of pure water vapour. The reaction then proceeds from right to left.

$$Boudouard: \qquad 2CO \leftrightarrow C_s + CO_2 \tag{2.12}$$

$$Methane\,decomposition: \qquad CH_4 \leftrightarrow C_s + 2H_2 \tag{2.13}$$

$$Reverse\,gasification: \qquad CO + H_2 \leftrightarrow C_s + H_2O \tag{2.14}$$

Boudouard and methane decomposition reactions are both catalysed by nickel. The respective reaction equilibria for the three carbon deposition reactions are shown in figures 2.7 - 2.9. While carbon formation through Boudouard and the reverse gasification reaction is promoted at low temperatures, methane decomposition gains significance at high temperatures. The possibility of coke depositions in the process can therefore not be completely eliminated and must be evaluated at a given operating point.

$$S/C = \frac{y_{H_2O}}{y_{CH_4}} \tag{2.15}$$

Deposited carbon can have different appearances inside the reactor. Important parameters, which determine the probability of coke formation, are the operating temperature and the steam to carbon ratio S/C. The inlet S/C ratio for this work is determined by the feed composition as shown in equation (2.15). The risk of carbon formation increases at lower S/C values. At high temperatures, carbon can form in a whisker-like shape [13]. Whisker-carbon has a graphitic structure, but may be formed even when there is no thermodynamic potential for graphite formation [15]. The generated carbon filaments may exert strong forces on the catalyst packing, which subsequently leads to a breakdown of particles. Consequently, the bed porosity decreases, leading to a higher pressure drop through the packed bed. When carbon is accumulated, partial or total blocking of the fixed bed can

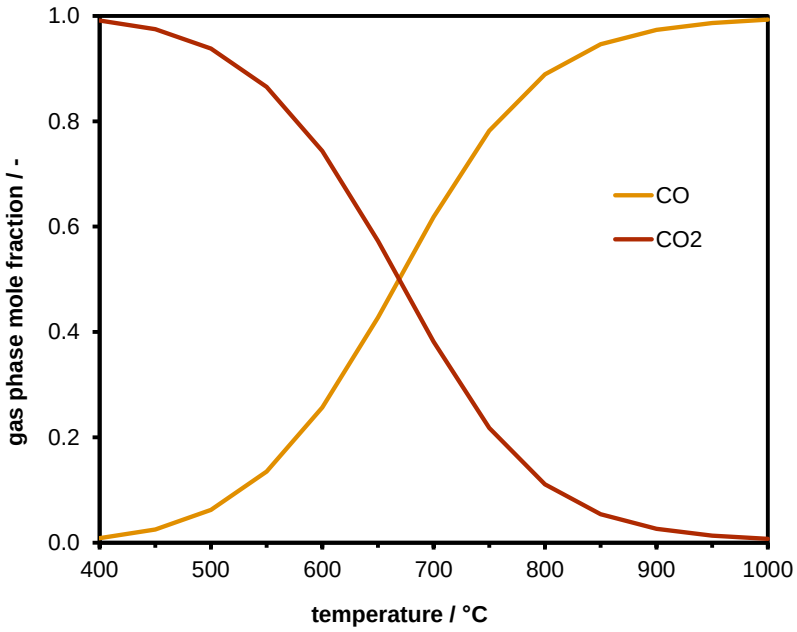

Figure 2.7.: Boudouard reaction equilibrium as a function of temperature.

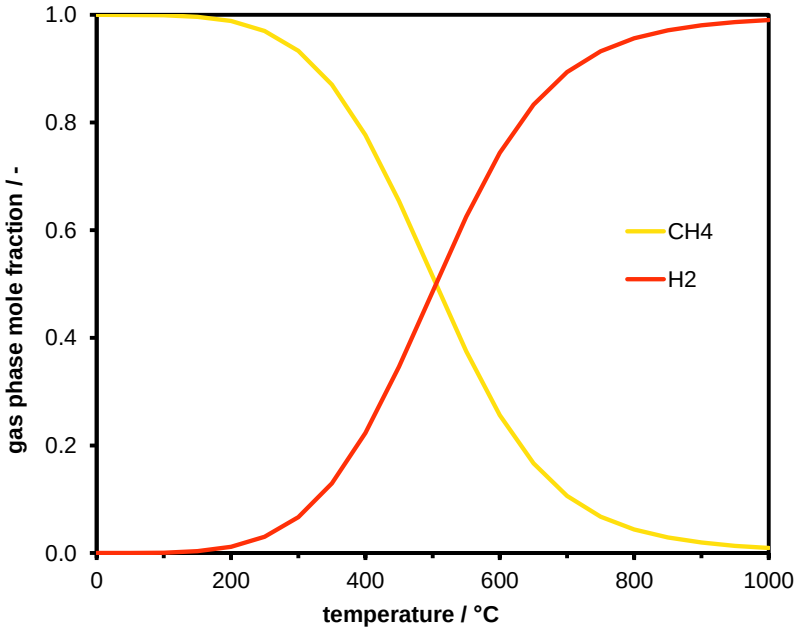

Figure 2.8.: Methane decomposition reaction equilibrium as a function of temperature.

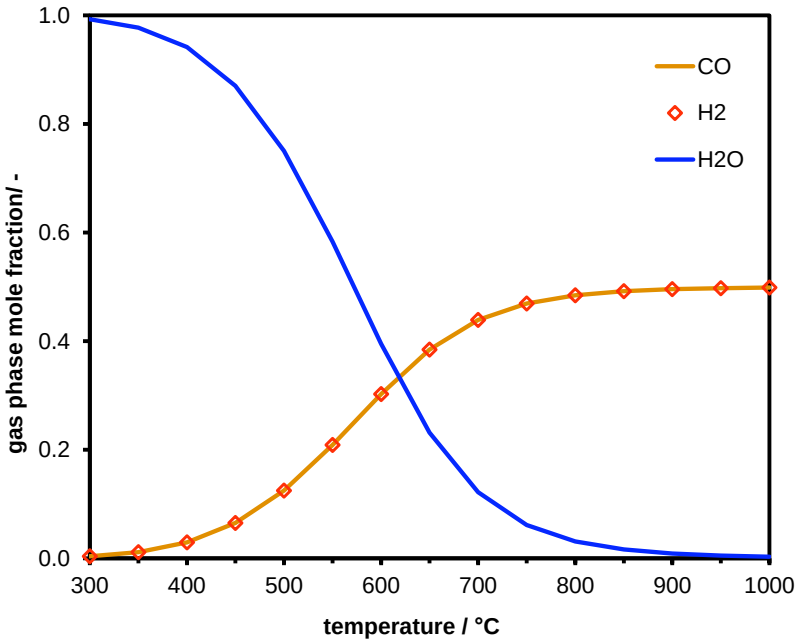

Figure 2.9.: Reverse carbon gasification reaction equilibrium as a function of temperature.

result from whisker-carbon formation and the catalyst has to be replaced. Whisker-carbon deposition is more likely to happen when the catalyst activity for the reforming reactions is low. However, this type of carbon formation does not inhibit the active sites and thus not does reduce the catalyst activity [13].

Other types of carbon formation are so-called encapsulating carbon and carbon formed by thermal cracking (pyrolytic carbon). When the local temperature is low, polymerisation of hydrocarbons into an encapsulating film around the particle can occur [13]. This leads to a progressive deactivation of the catalyst and reduces its activity. Pyrolytic carbon is promoted by high temperatures, but combines the effects of both prior-mentioned carbon types by deactivating the catalyst active sites and destroying the particles. It is formed by thermal decomposition of methane following reaction (2.13). High-porosity catalyst beds are more prone to this type of carbon deposition mechanism. If catalyst systems with acidic compounds are used, for example certain alumina supports, carbon formation by decomposition is more probable. Methane decomposition reportedly happens in regions with high heat fluxes, for example close to the tube wall where the reforming reactions are far from equilibrium [13]. Moreover, the formed pyrolytic carbon can cover the tube walls and reduce the local heat transfer coefficient.

The probability of carbon deposition can be regarded as a function of feed composition, operating pressure and local temperature. Generally, the risk of coke formation decreases when S/C is high. It has been reported that carbon formation by decomposition of methane

mainly occurs in regions with low hydrogen concentrations [15]. As hydrogen is quickly formed after the feed gas is supplied to the reactor, methane decomposition is most likely to happen at the beginning of the catalyst bed. Due to big radial temperature gradients, which often occur in the reactor, especially in the first few catalyst particle layers, local areas with potential for carbon formation can originate. Different carbon types may be formed depending on whether these are low or high temperature regions. Generally it can be stated that carbon deposition is governed by the relative kinetics of carbon-forming and carbon-removing reactions (gasification).

In order to avoid coking during the reformer operation, the operating parameters have to be chosen with care. Areas with low oxygen and hydrogen fractions, but high amounts of carbon should be avoided [21]. Catalysts that show sufficient activity for reforming and high selectivity towards gasification reactions to enhance the removal of deposited carbon should be used. Nickel catalysts have to be activated when the reforming process is started. Small amounts of hydrogen in the feed gas can have a positive effect on the activation [13]. A common method to do this is the regeneration with steam according to the reversal of reaction (2.14) [13]. However, it is possible that not all carbon can be removed by this process step. Another option is to burn off carbon depositions with air. As this reaction is highly exothermic, special care must be taken to avoid over-heating of local regions inside the reactor and cause sintering of the catalyst [13]. The adaption of operational strategies can be a useful method to avoid or reduce coking [17]. Limits regarding S/C feed ratios can be obtained from equilibrium evaluations. These limits, however, do not guarantee a carbon-free operation, as kinetic effects might still promote carbon formation.

Finally, changing or manipulating the catalyst material can reduce the risk of carbon formation. The choice of catalyst material should be made after evaluating several important features: resistance to coking and pure steam, inactivity for side-reactions, high activity even at high temperatures, mechanical strength and good heat transfer properties [18]. At high temperatures sintering occurs on nickel surfaces, which can lead to a loss of active catalyst surface [13]. Alternatives to the commercially established nickel catalyst are ruthenium and rhodium [17], which are more resistant to carbon formation, but much more expensive and therefore not often used in large applications. Several manipulations of Ni catalysts were reported in the past. Higher resistance to coking was achieved through the addition of potassium [15] and tin [22] to the catalyst and alloy-formation of Ni and Bi [17]. The choice of catalyst support also influences the resistance during the process. Common support materials are α-alumina, Mg, Mg-Al spinel, zirconia and cerium [13, 20]. When α-alumina is used, catalyst and support can form undesired $NiAl_2O_4$ compounds [13]. The addition of rare earth oxides to the support can favour the gasification reaction and reduce the

amount of carbon in the reactor [22]. Finally, the ensemble size control method is a means to reduce the probability of coking [22]. As carbon depositions need large associated surface areas and several active sites located next to each other, the active surface sites on each ensemble can be limited in order to avoid large active surface regions. Reforming reactions can also be catalysed on smaller ensembles, so this method increases the selectivity of reforming over carbon deposition reactions.

2.3. Computational Fluid Dynamics

With the evolvement of the personal computer and its constantly improving calculational capabilities, the field of computational fluid dynamics (CFD) has received increased attention over the last few decades. While researchers had to solve equation systems in a time-consuming manual process in the past, nowadays calculations can be made in a fraction of the time. In order to obtain physically feasible results, the used numerical methods must be selected with care and the simulation results always be validated against experimental data. If done correctly, CFD can be a strong aid to reactor design and the enhancement of process understanding. On the following pages, only the most significant theoretical aspects of CFD modelling are addressed. The finite volume method (FVM) is introduced and spatial discretisation described briefly, before an overview of turbulence modelling using the k-ε-model is provided. More details about numerical methods will not be presented in this work and can be found in the literature and the Ansys Theory Guide [23].

After determination of the mathematical model, which describes the regarded reactor system, it must be decided how the system of equations is solved. The appearance of non-linear equations needs to be addressed, as it makes analytical solutions impossible. This being said, numerical solution processes can also be reasonable methods for equation sets which can be solved analytically. The first step in a numerical solution process is the discretisation of the equation system. The finite volume method (FVM) divides the system geometry into many small cells, in which the equations are solved. Two adjacent cells share a common face, through which the values of calculated quantities are communicated. For a 2D system, the finite volumes are simplified to finite areas. The equations for each cell must then also be discretised in order to be able to calculate values for each cell. The FVM requires approximations for integrals, gradients and interpolations between cells. Numerical methods have to be used in order to approximate these mathematical operations. Prominent methods for gradients are the Green-Gauss approach and the least-square cell based algorithm. As the equations are always solved in the node of the cell, interpolations must be performed in

order to obtain values at the cell faces.

The Navier-Stokes equations describing mass and momentum transport only offer analytical solutions for certain simple flow regimes. In the field, geometries are often complex and several physical phenomena occur side by side, influencing each other. In order to still be able to evaluate the Navier-Stokes equations for such systems, Reynolds proposed a method that distinguishes between mean and fluctuating parts of variables, the so-called Reynolds decomposition. While mean quantities can be solved easily, the fluctuating share corresponds to turbulent flow patterns, which require great computational effort for their compilation. Therefore, these terms are often simplified and approximated by using so-called turbulence models. When this decomposition method is applied to the Navier-Stokes equations, the Reynolds averaged Navier-Stokes equations (RANS) are obtained. The RANS equations are a set of unclosed equations, containing the Reynolds stress term, which must be modelled in order to close the equations. This requirement results from the nature of the Reynolds stress term, as it introduces a coupling of mean and fluctuation variable parts and cannot be determined analytically [24]. Physically, the term describes the average momentum flux, which results from fluctuations of velocity.

The method of closing the Navier-Stokes equations is called turbulence modelling. While there are several different approaches, the methods being based on the Boussinesq approximation will be referred to in more detail, as this approach was also used for this work. The Boussinesq approximation assumes that the Reynolds stress tensor compounds are proportional to the mean velocity gradients and subsequently, turbulent momentum transport is a diffusive process [24]. This process can be described by introducing a new variable, the turbulent viscosity μ_t. A turbulence model can then be regarded as a set of transport equations, which is needed to determine the size of the turbulent viscosity. In the literature, much attention is granted to models, which utilise two equations to compile μ_t. A prominent example of a two-equation turbulence model based upon the RANS equations is the k-ε-model. The first equation describes the transport of turbulent kinetic energy k. In order to be able to close the k-equation, another transport equation defining the energy dissipation of turbulent energy ε has to be solved. The k-ε-model is applicable for a wide range of flow regimes and very common in fixed-bed reactor simulations. It represents a good compromise between applicability and quick-solving for many CFD problems [24].

3. Model Development

The aim of the studies behind this work was to develop a mathematical model that accurately describes a steam reforming process in a tubular reactor of industrial-scale diameter. Therefore, all occurring physical phenomena had to be taken into account and their influence on the solution was assessed. In this chapter, a detailed description of all assumptions, sub models, operating parameters and boundary conditions used for the simulation of the reformer is presented. Special consideration is granted to the representation of the catalyst bed as well as to the treatment of chemical reactions. Finally, insight into the applied solution strategies is provided.

The prototype model represents a reactor from the laboratory, which was used for prior studies by Nestl. The tubular reactor has a diameter of 36 mm and is illustrated in figure 3.1. It contains a reforming section and a part filled with the oxygen carrier. Details about the structure of the model are provided in this chapter. The scale-up of the prototype lead to the design of the reactor presented in figure. 3.2. Diameter (120 mm) and length of the reforming section were adopted from the used values in the model and only slightly modified. The reactor was then built and is available to validate the simulation results.

In order to evaluate the system of equations, a computational fluid mechanics (CFD) model was generated using the commercial software package Ansys Fluent 17.0, which was utilised for geometry design and meshing as well as the calculation process. The program operates on a 64-bit system under Windows 7. The used computer holds 16 GB RAM and two Intel Xenon 3 GHz processors with two cores each. Calculations were performed in parallel operation on all four cores. The computer was kindly provided by the Institute of Chemical Engineering and Environmental Technology for the duration of the research activities performed for this work.

The first step of the modelling process requires the definition of main simplifications, which can be made without compromising the result. The steam reforming process was performed in a symmetric tubular reactor with a constant inner diameter, which was filled with cylindrical catalyst pellets. The characteristic quantity N, describing the ratio of the tube inner diameter

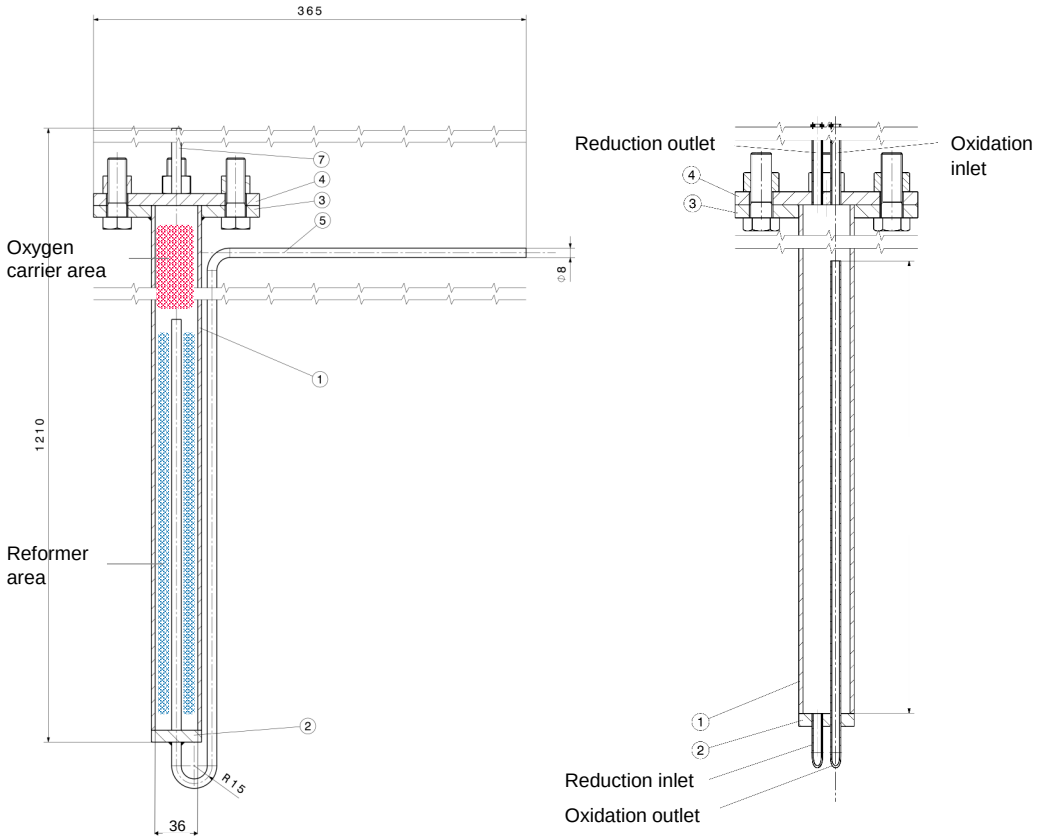

Figure 3.1.: Technical drawing of the RESC laboratory prototype reactor. Simulation results of a model of this reactor were validated with experimental results [11].

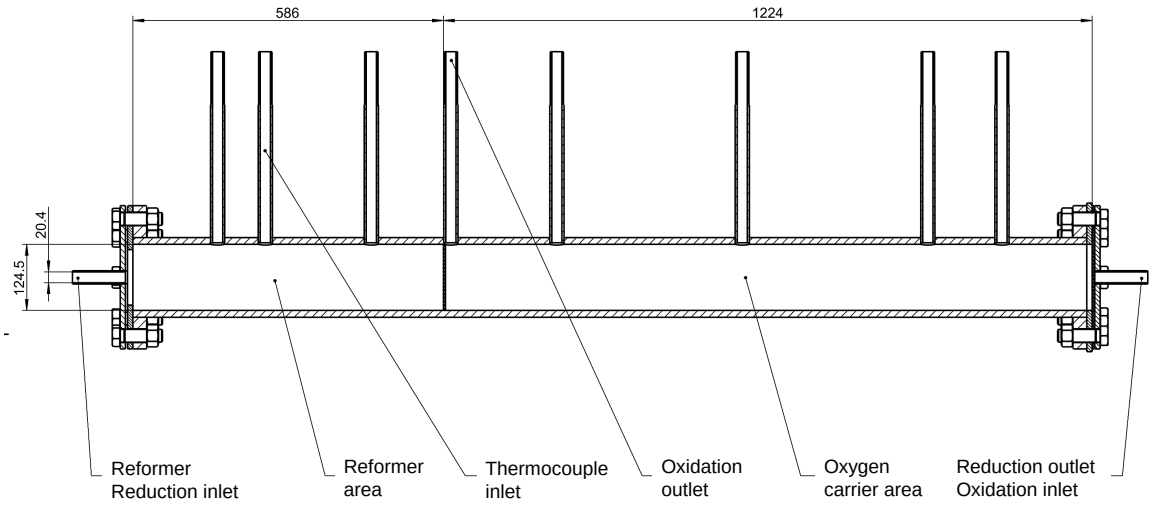

Figure 3.2.: Technical drawing of the RESC reactor with industrial-scale diameter. The construction of this reactor followed the studies presented in this work.

to the catalyst particle diameter, was introduced (equation (3.1)). The dimensionless quantity N can be regarded as a weighting factor, comparing the importance of macroscopic flow effects over single particle effects.

$$N = \frac{d_I}{d_p} \tag{3.1}$$

Past studies have shown the importance of particle configuration and wall flow effects for applications with low values of N, for example $2 < N < 6$ [25–27]. For high values of N however, as can be found in this work, the porous bed was assumed to have an isotropic structure, as single particle effects are of minor importance to the solution. Additionally, plug flow was assumed, as the influence of wall effects is small in comparison to the overall flow pattern when N is large [28]. The influence of gravimetric forces in the momentum equations was neglected as species densities were of similar magnitudes, the species were gaseous and the porous particles were considered rigid. In order to reduce the computational effort, the constant diameter of the reactor allowed the assumption of axisymmetry. Thus, the 3D system was treated as a two-dimensional system with axisymmetric properties.

As shown in the governing reaction equations (2.9 - 2.11) described in section 2.2, CH_4, H_2O, H_2, CO and CO_2 can be found in the process. Furthermore, N_2 was added to the feed gas, which serves two main purposes: Firstly, N_2 acts as an internal standard in MSR experiments, which is why it was also incorporated it into the model. Secondly, the used software Ansys Fluent requires a bulk species in order to maintain the validity of the continuity equation. For this purpose the last species equation is used to close the mass balance in the model and is therefor calculated from the sum of the residual species. Due to its inert character, N_2 was used to stabilise the numerical solution process by functioning as the bulk species in the present model.

An essential feature of an accurate mathematical model in chemical engineering is the correct representation of temperature-dependent physical properties. To that end, physical properties of the gaseous species were considered variable with local temperature. Heat capacity was modelled using a piecewise-polynomial approach, which is enabled by default in Ansys Fluent. Species thermal conductivity and viscosity were treated as piecewise-linear functions, with incremental values adopted from the literature [29]. For methane, the density is calculated using the Peng-Robinson equation of state. The dynamic viscosity of methane relates from a fourth degree polynomial approach, which was included in the model [29]. For the second feed component, water in its vapourous form, partial linear interpolation approaches were set for the calculation of density and dynamic viscosity. For

an accurate representation, 16 data points ranging from 100 °C to 800 °C were taken from the literature and provided for the density and dynamic viscosity determination [29]. VDI presents these data points as results of calculations with the IAPWS-IP97 equation. The data for the feed species, water and methane, was partly adopted from VDI Wärmeatlas and partly calculated using the empirical equations listed there. All further properties and mixing laws, such as molar masses and standard state properties, were left at their default values. Density, thermal conductivity and viscosity mixing follow an ideal gas approach, while for heat capacity the Fluent default mixing law was used, which calculates the mixture quantity in a linear way using species mass fractions. A description of the solid catalyst material can be found in section 3.2.

3.1. Geometry and Meshing

The first step in the realisation of a CFD model is the generation of a geometric domain and a suitable computational mesh, which makes the accurate and numerically stable evaluation of the equation system possible. Geometry and mesh design were performed in the respective design tools offered in Ansys Fluent. For reasons of improving the convergence behaviour, the reactor tube was divided into two sections: an inert zone and a catalyst bed. Both zones are filled with porous material of the same porosity, whereby reactions only take place in the second part. This discrimination made it possible to assign different attributes to the two zones. As mentioned before, the geometric domain was considered two-dimensional and in order to reduce the computational domain, only half of the cross-section, which is the profile between wall and rotational axis, was modelled.

Heat transfer through the reactor wall was taken into account by applying a boundary condition at the inner wall. The temperature profile in the wall and, subsequently, the treatment of the heating device was not considered in this work. Therefore, thermal conduction through the wall itself is not treated in the model (see section 3.6) and the reactor walls not implemented in the geometry design process. All attibuted component names are summarised in figure 3.3. It is important to mention, that no umlauts must be used in component names. Therefore, the inside of the reactor is named schalenkoerper and not schalenkörper.

The geometries for the prototype and the industrial-scale reactor were set up according to the considerations stated above. For the prototype, the dimensions of the laboratory reactor used by Nestl in his studies were adopted, as was the point of division between inert region and catalyst bed [11]. The dimensions for the reforming section of the RESC reactor were

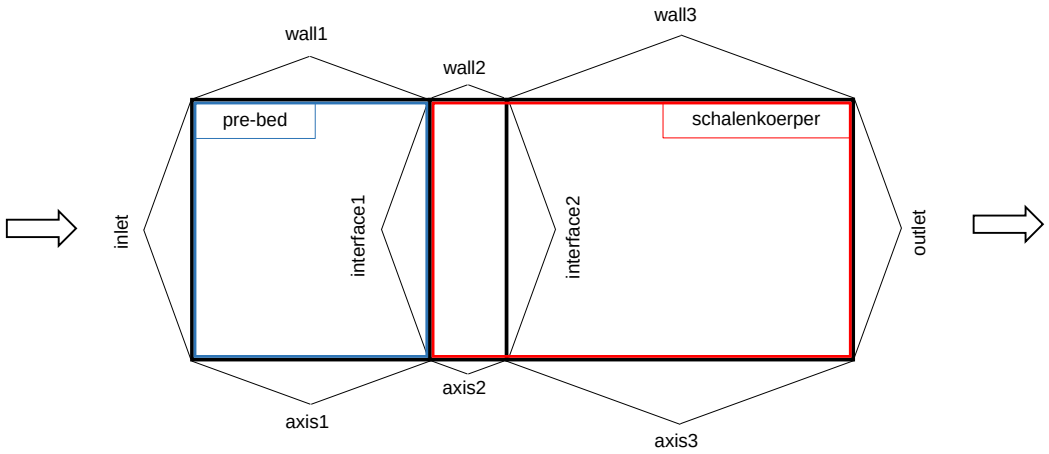

Figure 3.3.: Definition of component names as used in the model. By distinguishing between components, different attributes can be assigned to them during the model setup process.

guided by the diameter of an industrial reactor, whilst the length of the section was limited by the available space inside the application due to its utilisation purpose in a RESC application (see section 2.1) [5, 14]. The main geometric characteristics for both reactors have been summarised in table 3.1.

In order to create a fine computational grid, which enables the calculation of a precise result, but is coarse enough to avoid unnecessary small cells, a suitable meshing strategy was developed. For both reactors the catalyst bed was divided into a finely resolved zone at the beginning of the catalyst bed and a coarser following section before the outlet of the reactor. The need for this differentiation was driven by the expectation of high reaction rates and large gradients in the beginning of the bed, as reaction activity prevails in the first catalyst layers. This was later confirmed by reaction rate results and the strategy was therefore maintained throughout the studies. The high resolution in the finely meshed zone was made possible by limiting the element size of the respective zone to a maximum possible value. Different element size restrictions were set for the distinguished regions, as visible in figure 3.4 (a), where the transition of a coarser mesh in the pre-bed towards a higher resolution in the catalyst section is depicted. Besides coarse element sizes in the pre-bed and the rear section of the reformer, cell sizes were also limited at the reactor wall in order to keep the maximum aspect ratio in the first layers near to the wall low and thus promote the stability of the solution process.

In addition to different element size restrictions for different zones, an inflation layer condition was applied at the wall, which has been illustrated in figure 3.4 (b). The inflation layer method defines the height of the first cell adjacent to the wall and the growth rate towards the reactor axis. The inflation layer was used for the reactor wall, allowing different maximum layer

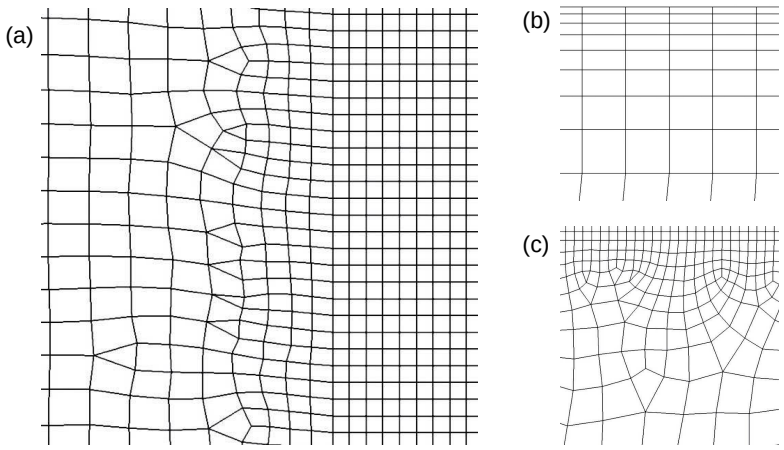

Figure 3.4.: Computational grid details of the large reactor: (a) transition zone from pre-bed to finely-meshed beginning section of the catalyst bed, (b) inflation layer at the reactor wall, (c) the subsequent increase of cell size requires the incorporation of triangular cells.

heights depending on the local resolution of the mesh. The cell size increases towards the reactor axis until it reaches the maximum value pre-defined by the respective element size restriction. This cell growth leads to a distortion of the rectangular cells and the inclusion of triangular cells (see figure 3.4 (c)) in order to keep the aspect ratio sufficiently low. As the Enhanced Wall Treatment (EWT, see section 3.6) is used, the maximum size of the first cell layer is given by the restriction, that y^+, defined as depicted in equations (3.2) - (3.3), must not exceed unity [23]. As visible in the equation, y^+ is a function of phyiscal properties, radial position and friction velocity u_τ. As density and dynamic viscosity appear in the equation, y^+ is therefore also temperature-dependent. The friction velocity is a function of the local shear stress at the wall and the density of the fluid. With the abovementioned settings applied, the characteristics of the resulting mesh have been summarised in table 3.2.

$$y^+ = \frac{\rho \cdot u_\tau \cdot y}{\mu} \tag{3.2}$$

$$u_\tau = \sqrt{\frac{\tau_w}{\rho}} \tag{3.3}$$

Lastly, to ensure the independency of the results from the resolution of the mesh, a mesh independence study (MIS) was conducted for the prototype reactor. For that purpose, the simulation was repeated several times with consequently reduced mesh sizes until further refinement had no influence on the results anymore. This mesh quality was then used for all

Table 3.1.: Summary of geometric features of the prototype and the industrial-scale diameter reactor.

Quantity	Prototype	Reactor	Unit
Diameter	36	120	mm
Total length	205	600	mm
Length of catalyst bed	105	400	mm
N	11.3	37.8	-

Table 3.2.: Main characteristics of the computational grid generated for the prototype and the industrial-scale reactor.

Quantity	Prototype	Reactor	Unit
Cells	82,000	73,000	-
Maximum aspect ratio	25.16	7.483	-
Minimum orthogonal quality	0.271	0.401	-
Maximum y^+	0.0368	0.580	-

further prototype simulations.

3.2. Porous Media Model

The centrepiece of the reactor model is the replication of the porous bed. Two ways of representing the catalyst region were considered: resolving each particle in a discrete manner or treating the bulk of particles as a continuum. A thorough evaluation showed some profound shortcomings of the discrete approach. Firstly, in order to achieve a representative result, the particles must be distributed randomly or, if not, many different particle configurations have to be examined. The consequence is a protracted series of experiments needed to achieve a meaningful result. Secondly, the computational expense of solving equations for the whole catalyst bed would have exceeded the available processing power. Thus, only a small section of the bed could be examined at a time. Lastly, also the generation of a discrete geometry and a respective mesh with sufficient accuracy is a very time-consuming process step.

Due to this evaluation of practicability, a pseudo-homogeneous modelling approach was chosen. The fixed-bed is considered a continuum and characterised by universal properties. The main parameters describing the pseudo-continuum are: porosity, inertial and viscous resistance coefficient, surface-to-volume ratio and coefficient of thermal conductivity. As

the model does not distinguish between single particles, lumped parameters are used for calculations. This inevitably leads to a non-physical simplification of the system, whereby the consequences can only be examined by validating simulation results with future data from laboratory experiments. This assumption creates limitations of the pseudo-continuum approach for the treatment of thermal radiation, fluid-particle heat transfer as well as proper description of the velocity profile in the model. The latter results in a slight deviation in the prediction of enthalpy transport, which is then brought into the energy equation. One further consequence is the wrong prediction of convective and diffusive flow and a subsequent exaggeration of heat transfer [28]. This numerical interpolation effect then makes it impossible to satisfy the non-slip condition at particle surfaces, thus slightly modifying the velocity profile. However, the influence of the pseudo-homogeneous simplification on the overall energy balance, on which the focus is laid, is considered to be small [30]. Therefore, it is assumed that the resulting uncertainties only have a small impact and the representation of the reactor system is still of acceptable significance.

As the model was designed for the evaluation with the software Ansys Fluent, many of the procedures described in this section make use of information provided in the Ansys Fluent User's Guide [31]. For a more detailed description, refer to section 6.2.3 of the User's Guide.

In order to take the influence of porosity on the fluid velocity into account and therefore accelerating the flow with decreasing porosity, equations were framed using the physical velocity formulation. The porosity of the fixed-bed ε can be calculated from the catalyst bulk density and the density of a single particle (equation (3.4)). It characterises the ratio of void space to total catalyst bed volume. The calculated value for porosity is of great importance to the model. It shows in pressure drop and flow velocity evaluations, for instance, as well as in the compilation of lumped parameters. The porosity for the performed studies was considered constant.

$$\epsilon = 1 - \frac{\rho_f}{\rho_p} \tag{3.4}$$

Another important parameter characterising the flow through a random catalyst packing is the resistance of the bed. By evaluating the flow through the catalyst bed, utilising coefficients of viscous and inertial resistance, the pressure drop ΔP can be determined using the Ergun equation depicted in equation (3.5). Ergun defines the pressure loss through a packed bed as the sum of inertial and viscous losses (equation (3.6) - (3.10)) [32]. The equation contains dependencies on the length of the packing L, the parameters bulk velocity U_∞,

porosity and particle diameter as well as the dynamic viscosity μ, which itself is a function of temperature. The resistance coefficients can directly be derived from the equation and calculated by inserting the particle diameter and the porosity of the bed [31].

$$\frac{\Delta P}{L} = 150 \cdot \frac{(1-\epsilon)^2}{\epsilon^2} \cdot \frac{\mu \cdot U_\infty}{d_p^2} + 1.75 \cdot \frac{L \cdot \rho}{d_p} \cdot \frac{1-\epsilon}{\epsilon^2} \cdot U_\infty \cdot |U_\infty| \tag{3.5}$$

$$\Delta P = \Delta P_{viscous} + \Delta P_{inertial} \tag{3.6}$$

$$\Delta P_{viscous} = C_{viscous} \cdot \mu \cdot U_\infty \tag{3.7}$$

$$\Delta P_{inertial} = \frac{\rho}{2} \cdot C_{inertial} \cdot U_\infty \cdot |U_\infty| \tag{3.8}$$

$$\frac{1}{C_{viscous}} = \frac{d_p^2}{150} \cdot \frac{\epsilon^2}{(1-\epsilon)^2} \tag{3.9}$$

$$C_{inertial} = \frac{3.5}{d_p} \cdot \frac{1-\epsilon}{\epsilon^2} \tag{3.10}$$

As fluid-particle heat transfer was considered fast, it was assumed, that the fluid and solid regions are in constant thermal equilibrium. The definition of the lumped coefficient of thermal conductivity is shown in equation (3.11).

$$\lambda = \epsilon \cdot \lambda_f + (1-\epsilon) \cdot \lambda_s \tag{3.11}$$

For completion of the porous media model the catalyst must be characterised. The catalyst modelled for the simulation was utilised in the prior prototype experiments by Nestl and the value for catalyst bulk density was adopted from his work [11]. The weight and the dimensions of ten cylindrical particles were measured and the particle density calculated from the average results. The particles are made of Al_2O_3 and coated with Nickel. However, for reasons of simplification, a lumped particle density was used, rather than distinguishing

Table 3.3.: Summary of characteristic features of the catalyst bed.

Quantity	Size	Unit
Diameter	3.175	mm
Length	3.175	mm
Al_2O_3 density	1,711	$kg \cdot m^{-3}$
Catalyst bulk density	1,000	$kg \cdot m^{-3}$
Porosity	0.416	-
S/V	1,890	m^{-1}

between the two materials. This also applies for the values for heat capacity and thermal conductivity, where the influence of the Nickel layer was neglected and literature data for Al_2O_3 used for the model [29]. For the determination of the surface-to-volume ratio S/V, particle length and diameter of 3.175 mm each were used. Due to the full cylindrical shape of catalyst particles, a S/V value of 1890 m^{-1} was computed. An overview over the parameters characterising the catalyst bed can be found in table 3.3.

3.3. Mass and Momentum Equations

Mass und momentum transport through the porous region is described by the continuity equation and the Navier-Stokes equations for Newtonian fluids. The examined process is stationary and axisymmetric, hence all temporal derivatives and angular gradients must be equal to zero. Due to chemical reactions and strong variation of the temperature inside the reactor, the fluid is considered compressible, which results in the formulation of the continuity equation as reported in equation (3.12), with porosity assumed to be constant and therefore eliminated from the equation.

$$\nabla(\rho \cdot \vec{v}) = 0 \tag{3.12}$$

The Navier-Stokes equations can be written with the Brinkman extension as shown in equation (3.13) [16, 31]. The extension term accounts for the drag force induced by the catalyst bed, utilising the constant resistance coefficients derived from the Ergun equation for solid particles (see section 3.2). Again, all temporal derivatives and angular gradients are equal to zero. As the bed porosity is treated as a constant, it can be eliminated from the first three terms of the momentum equation and only shows in the drag force terms. Temperature

dependencies occur in the equation due to the influence of density ρ, dynamic viscosity μ as well as pressure p. The definition of the stress tensor is described in equation (3.14). The first term takes the viscosic behaviour of the fluid into account, the second determines the effect of volume expansion due to local stresses [23].

$$\nabla(\rho \cdot \vec{v} \cdot \vec{v}) = -\nabla p + \nabla(\vec{\tau}) - (C_{viscous} \cdot \epsilon \cdot \mu \cdot \vec{v} + C_{inertial} \cdot \frac{\epsilon^2}{2} \cdot \rho \cdot |\vec{v}| \cdot \vec{v}) \tag{3.13}$$

$$\overline{\tau} = \mu((\nabla\vec{v} + \nabla\vec{v}^T) - \frac{2}{3}\nabla \cdot \vec{v}I) \tag{3.14}$$

From left to right the terms of equation (3.13) account for: convective momentum transport, changes in pressure, the stress tensor gradient and the two body forces imposed by the porous medium. The influence of chemical reactions will manifest itself in an alteration of the local density and have been further addressed in section 3.5.

The evaluation of the Navier-Stokes equations requires a supplementary treatment of turbulence in order to be able to compute the Reynolds stress tensor, which can only by solved analytically for certain simple flow fields. For this work, the RNG k-ε model, first introduced by Launder and Spalding, was used [33]. The model solves two additional transport equations, one for the turbulence kinetic energy k and one for its rate of dissipation ε and is extended with a renormalisation group (RNG). The RNG group accounts for low-Reynolds effects and extends the applicability of the k-ε model to lower Reynolds numbers [23]. The k-ε turbulence model is a common choice for fixed bed reactor simulations [26, 28, 34, 35].

3.4. Energy Equation

The energy transport in the system is described by the energy equation (3.15). All temporal derivatives equal zero, as the process is assumed to be stationary. The left term in equation (3.15) represents the change of total energy (enthalpy and kinetic energy) in the system. The terms on the right side of the equation describe the mechanisms causing this change of total energy. From left to right they stand for: the change of enthalpy due to chemical reactions, energy transport through thermal conduction, energy transport via diffusion and viscous dissipation losses. The strain rate can be described as analogous to previously

shown in section 3.3.

$$\nabla \cdot (\vec{v} \cdot (H_f + \rho_f \cdot \frac{\vec{v} \cdot |\vec{v}|}{2})) = \sum_j \Delta H_{r,j} + \nabla \cdot [\lambda \cdot \nabla T - (\sum_i h_i \cdot J_i) + (\overline{\overline{\tau}} \cdot \vec{v})] \tag{3.15}$$

The temperature in the reactor depends on several interconnected mechanisms. Firstly, energy is drawn from the process for the conversion of methane to hydrogen. As the reforming reactions lead to a volume growth, the local pressure increases, which also influences the flow velocity according to Bernoulli's theorem. As soon as a temperature gradient inside the reactor occurs, energy is transported via thermal conduction against this gradient, aiming to reduce temperature differences. External influence on the energy balance comes from diffusional fluxes and conversion of energy into heat by means of viscous dissipation. Above all, it can be seen that the temperature inside the catalyst bed results from a functional interaction of several mechanisms.

In order to promote the understanding of the process, the main dependencies between variables and parameters must be understood. At the heart of the simulation are the two main variables: temperature and the rates of the three governing reactions. These variables influence each other, as the reaction rates vary with temperature and consume energy, thus retracting energy and lowering the temperature. Additionally, the volume growth induced by the reactions influences the local pressure and the fluid composition changes when reactions occur, leading to changes in fluid properties (ρ, λ, μ, c_P, D). The second major variable, temperature, causes changes of the physical properties of the single species. Subsequently, this also influences properties of the gas mixture. Alterations of physical properties of the mixture then trigger changes in all equations where they are used, such as, for example, in pressure and velocity variations due to the momentum equation.

It was assumed that heat transfer mainly happens through the processes of thermal conduction, convective and diffusive enthalpy transport. The influence of thermal radiation on the overall energy balance was not examined in this work. This being said, it can not be ruled out that heat transfer through radiation processes might further improve the quality of the solution. However, the software used does not offer means to model radiation in porous media for low porosities, as the interaction between radiation and the solid bed cannot be represented in a correct manner [23]. The implementation of a valid radiation model is seen as an important task for further improvement of the given model structure.

Several submodels were included as extensions of the equation of energy. [23]. Firstly,

as mentioned in section 3.2, fluid and solid particles are considered to be in thermal equilibrium. Thus, the temperature of the solid material and the fluid are equal, which leads to simplifications in the energy equation. Secondly, thermal diffusion effects were considered. These include enthalpy transport by diffusion and varying diffusion velocities for molecules with different molecular masses. Therefore, heavy molecules diffuse slower towards heated surfaces. Diffusion is described with the Stefan-Maxwell equations in a full multicomponent diffusion model [31]. The result of the diffusion equations is incorporated into the energy equation as a set of diffusive species fluxes (J_i in equation (3.15)). Lastly, thermal effects on the velocity profile in the vicinity of the wall were taken into account as an extension of the EWT model (addressed in section 3.6). Thus, the influence of the increased wall temperature on near-wall flow is accounted for. The exact equations for these used submodels can be found in the User's Guide section 7.9.2.2. (Stefan-Maxwell equations), 7.9.4. (thermal diffusion coefficients) and the Theory Guide section 4.14.5.2 (EWT thermal effects) [23, 31].

3.5. Chemical Reactions

The accurate representation of chemical reactions in the reformer is of great importance to the quality of the model. Three governing reactions (2.9) - (2.11) were taken into account and incorporated into the system model with a kinetic model approach first suggested by Xu and Froment, which is widely used and accepted in methane steam reforming modelling and simulation [35–40]. The reaction rate model describes the three governing reactions in methane steam reforming as functions of the local composition, temperature and pressure. The model was developed on a $Ni/MgAl_2O_4$ spinel catalyst, however, it is often applied for Ni/Al_2O_3 catalyst investigations as well [37, 39, 40]. The used equilibrium constants were adopted from Sadooghi and Rauch [30].

In order to be able to utilise the reaction rate model in Fluent, a user-defined function (UDF) was implemented. The function was written in C/C++ and can be found in the appendix of this work. Several rules must be followed to ensure the performance of the function. Initially, the macro "DEFINE_VR_RATE" must be used at the beginning of the function. Before calling the macro, the file "udf.h" has to be included into the function. To translate the function to the language used by Ansys Fluent, Microsoft Visual Studio must be installed on the computer and its use enabled in Fluent. It is essential that Ansys Fluent is started through the Windows System Development Kit (SDK) Command Prompt, in order to be able to compile the UDF. The UDF file must then be compiled (not interpreted) into Fluent. The

integration of a UDF file must be done carefully and reference to the respective UDF Manual for further information on the matter is recommended [41].

The reaction rates of MSR reactions (2.9) - (2.11) are respresented in the model as shown in equations (3.16) - (3.19). Reaction r_1 describes the reforming reaction to H_2 and CO (reaction (2.9)), r_2 represents the water-gas shift reaction (reaction (2.10)) and r_3 the reforming reaction to H_2 and CO_2 (reaction (2.11)).

$$r_1 = \frac{k_1}{p_{H_2}^{2.5}} \cdot (p_{CH_4} \cdot p_{H_2O} - \frac{p_{H_2}^3 \cdot p_{CO}}{K_1}) / (DEN)^2 \tag{3.16}$$

$$r_2 = \frac{k_2}{p_{H_2}} \cdot (p_{CO} \cdot p_{H_2O} - \frac{p_{H_2} \cdot p_{CO_2}}{K_2}) / (DEN)^2 \tag{3.17}$$

$$r_3 = \frac{k_3}{p_{H_2}^{3.5}} \cdot (p_{CH_4} \cdot p_{H_2O}^2 - \frac{p_{H_2}^4 \cdot p_{CO_2}}{K_3}) / (DEN)^2 \tag{3.18}$$

$$DEN = 1 + K_{CO} \cdot p_{CO} + K_{H_2} \cdot p_{H_2} + K_{CH_4} \cdot p_{CH_4} + \frac{K_{H_2O} \cdot p_{H_2O}}{p_{H_2}} \tag{3.19}$$

All three equations share the same denominator DEN, which accounts for the adsorption of reactive species on the catalyst active sites. Since all three reactions are assumed to happen on the same active sites, the denominator is equal in all three equations [36]. The reaction rate constants are determined by using an Arrhenius approach. The corresponding values for pre-exponential factors and activation energies have been listed in table 3.4 [36].

$$k_1 = A(k_1) \cdot exp(\frac{-E_1}{R \cdot T}) \tag{3.20}$$

Equilibrium constants were included as shown in equations (3.21) - (3.23) [30].

$$K_1 = 10,266.76 \cdot exp(-\frac{26.83}{T} + 30.11) \tag{3.21}$$

Table 3.4.: List of pre-exponential factors and activation energies used for the determination of reaction rate constants in the implemented reaction rate model [36].

Reaction	A	E / kJ · mol^{-1}
r_1	$4.225 \cdot 10^{15}$	-240.1
r_2	$1.955 \cdot 10^{6}$	-67.13
r_3	$1.020 \cdot 10^{15}$	-243.9

Table 3.5.: List of pre-exponential factors and adsorption enthalpies used for the determination of adsorption constants in the implemented reaction rate model [36].

Species	A(K_i)	ΔH_i / kJ · mol^{-1}
H_2	$6.12 \cdot 10^{-9}$	-82.90
CO	$8.23 \cdot 10^{-5}$	-70.65
H_2O	$1.77 \cdot 10^{5}$	88.68
CH_4	$6.65 \cdot 10^{-4}$	-38.28

$$K_2 = exp(-\frac{4,400}{T} - 4.063) \tag{3.22}$$

$$K_3 = K_1 \cdot K_2 \tag{3.23}$$

Adsorption coefficients were calculated using a Van't Hoff approach, as visible in equation (3.24). The respective values for activation energies and adsorption enthalpies have been summarised in table 3.5.

$$K_i = A(K_i) \cdot exp(\frac{-\Delta H_i}{R \cdot T}) \tag{3.24}$$

3.6. Operation Parameters and Boundary Conditions

Subsequent to the setup of the model, a careful selection of boundary conditions was performed. For all prototype simulations, the experimental setup by Nestl was reproduced by adapting the boundary conditions to fit the operating parameters [11]. Mass flow and inlet composition were adopted and a small amount of hydrogen added to the feed. The reason

Table 3.6.: Inlet molar compositions (%) and S/C ratios for prototype and reactor simulations..

	CH_4	H_2O	H_2	N_2	S/C
Cycle 1	24.5	64.2	1.00	10.3	2.63
Cycle 3	27.2	66.0	1.00	5.88	2.43
Cycle 5	30.0	63.3	1.00	5.65	2.11
Reactor	42.7	51.3	1.00	5.00	1.2

Table 3.7.: Summary of boundary conditions for prototype and large reactor simulations: mass flow and wall temperature as well as pressure drop results.

	$\dot{m}_{in}$ / kg · h^{-1}	T_w / °C	ΔP / Pa
Cycle 1	$4.77 \cdot 10^{-2}$	807	45.3
Cycle 3	$8.13 \cdot 10^{-2}$	855	87.2
Cycle 5	$8.44 \cdot 10^{-2}$	857	92.3
Reactor	3.48	850	672

for this can be found in the structure of the reaction rate model equations. Some hydrogen must be present in order to avoid a division through zero in equations (3.16) - (3.18). The experiment inlet mass flow was therefore corrected to ensure same amounts of methane and water enter the reactor in both the prototype experiments and the simulations. The feed composition for the industrial-scale diameter reactor was set by using a S/C ratio of 1.2. As with the prototype, small amounts of hydrogen (1%) and nitrogen (5%) are added to the feed. The addition of nitrogen serves as an internal standard in order to facilitate future laboratory experiments. The total inlet molar flow was set as described in table 3.7.

Boundary conditions for the energy equation comprise the feed temperature and a thermal condition for the reactor wall. The goal of this work was the examination of the influence of the endothermic reactions on the temperature in the catalyst bed. It was assumed that the reactor wall has a constant temperature, which is equal to the temperature of the feed. For the prototype studies, average wall temperatures were calculated and adopted from the results of Nestl [11]. In the case of the reactor simulation, the constant wall temperature was assumed to be equal to 850 °C. The assigned values for inlet compositions and the respective S/C ratios have been summarised in table 3.6. A list of values for inlet mass flows, wall temperatures and resulting pressure drops is shown in table 3.7.

To address the quality of turbulence in the feed, inlet conditions for turbulent intensity and hydraulic diameter were set. The turbulent intensity of the feed can be estimated with equation (3.25) [31]. The hydraulic diameter is equal to the reactor diameter in a tubular

reactor (equation (3.26)). Turbulence was considered in order to facilitate future studies with higher feed flows, and thus larger Reynolds numbers and a bigger influence of turbulence on the flow field.

$$I = 0.16 \cdot Re_{d_H}^{-\frac{1}{8}} \tag{3.25}$$

$$d_H = d_i \tag{3.26}$$

At the reactor wall, a no-slip condition was applied. In conclusion, axial and radial velocity must be equal to zero at the wall. For an accurate representation of the viscous and the thermal boundary layer establishing in the vicinity of the wall, the Enhanced Wall Treatment (EWT) model was used. The EWT is the state of the art method to generate precise results near the wall [28, 39, 42]. By integrating a wall function into a two-layer model, it combines two traditional approaches to boundary layer treatment [23].

3.7. Numerical setup

Stability and necessary time for the iteration process are determined by the solver type used for the iteration process. For the evaluation of the equation system, a pressure-based, coupled solver with double precision floating point format was chosen. The pressure-based solver induces an additional pressure correction equation, which is necessary to close the equation system and must satisfy the equation of continuity. The coupled algorithm solves the system of momentum and continuity equations simultaneously, which leads to a higher memory requirement, but significant improvement of convergence rates [31]. Double precision was used, as it generally promotes convergence and the required additional computational domain could be afforded.

To enforce high stability during the calculation process while avoiding unnecessary computational cost suitable numerical methods were selected. Gradients were approximated using the least squares cell-based method. Pressure values at faces between cells were interpolated with the pressure staggering option (PRESTO). Spatial discretisation for the equations describing density, momentum, k, ε, species and energy was performed with an 2^{nd}-order upwind approach.

The first prerequisite for the attainment of convergence in a simulation is the decrease of residuals by a pre-defined amount of orders of magnitude. For the simulations in this work no lower residual limits were set, because at the times when the monitors reached constant values, the residuals usually had dropped by several orders of magnitude already. The second condition, which must be met for a converged solution, are constant monitoring variables. The quantities surveyed during the solution process must be expressive for the investigated simulation objectives. In case of this model, six monitors were set:

1. water inlet mole fraction
2. hydrogen outlet mole fraction
3. outlet mass flow
4. average coefficient of thermal conductivity in the catalyst bed
5. total heat input at the reactor wall
6. average reaction rate of reaction 3 (equation (2.11))

Monitor 1 observes the feed composition and can be regarded as a precaution against mistakes in the setup of the model. For monitor 2, the target value is calculated from a manual calculation of the feed composition using the stoichiometry of the reaction equations and assuming full conversion of methane and water. The surveilled value can then be compared and the convergence of this monitor judged. Monitor 3 gives information about the satisfaction of the continuity equation. The outlet mass flow must be stable at the feed mass flow value in order to ensure that mass is neither brought into or eliminated from the process by reasons of numerical phenomena. Monitors 4 - 6 all yield information to assess if a stationary operation point has been established. Experience showed that monitors 2, 4, 5 and 6 all reached their respective constant values around the same time and were the last to reach constant values. It was observed that the flow field needs fewer iterations in order to reach a stable operating point than the species distributions. As monitors 2, 4, 5 and 6 either directly or indirectly all describe the progression of chemical reactions, it can be said that the calculation time determining step of the simulation is chemical conversion.

During the first iterations, the residuals were high and influenced each other severely. In all simulations, under-relaxation factors (UF) were utilised to stabilise the solution process at the start. UF for species residuals were reduced down to 0.4 in order to avoid divergence, which was most likely to happen as a consequence of the behaviour of one of the species residuals. Due to sudden changes in the temperature distribution the temperature decreased rapidly, leading to high residuals, impossibly low temperatures and, furthermore, a diverging solution. This could be avoided by combining two strategies. Firstly, as already mentioned, low UF for species and energy residuals were used. Secondly, during the initialisation

process, methane fractions in the reactor were set to zero. As a further consequence, the methane content in the reactor increased slowly, iteration by iteration, which lead to the slower onset of chemical reactions, lower residuals and inhibited diverging behaviour. Sudden changes of local methane fractions could be avoided and the calculation process thus be stabilised.

4. Results and Discussion

In the following part calculation results are presented and discussed thoroughly. Before going into detail about the simulation results, thermodynamic equilibrium calculations are presented to create a basic understanding of the behaviour of the reactions and the influence of operating temperature and steam-to-carbon ratio (S/C) on the product composition. The interpretation of the simulations must always be performed on the basis of a validation procedure. Thus, the results of the prototype calculations are and compared to experimental data before discussing the large reactor. Conclusions are drawn in order to enable an interpretation of the dataset obtained from the industrial-scale reactor simulation. The deviations between prototype experiments and theoretical calculations are examined and possible model improvements addressed. With the conclusions drawn from the validation process, the reactor simulation results are then discussed. Special attention is granted to the observed temperature distribution inside the reactor and the associated energy demand as well as the composition of the fluid in the reactor and at its outlet. Furthermore, the probability of carbon formation during operation is addressed.

4.1. Thermodynamic Studies

Thermodynamic studies of synthesis gas compositions in a MSR process were conducted in order to estimate the carbon formation boundaries. Two calculations were performed at chemically equilibrated state. Firstly, the S/C ratio was varied at a constant operating temperature of 850 °C in order to assess the influence of the S/C ratio on carbon deposition boundaries. Secondly, the feed composition was set to a constant value and the temperature varied. The calculations were conducted with the software Aspen Plus by using the method of minimising the Gibbs free energy. As reactions can only occur when the Gibbs free energy decreases, a stable operating point is reached when the free energy reaches a minimum. This approach provides advantages over calculations of equilibrium constants when several reactions are considered simultaneously or more complex reaction mechanisms occur.

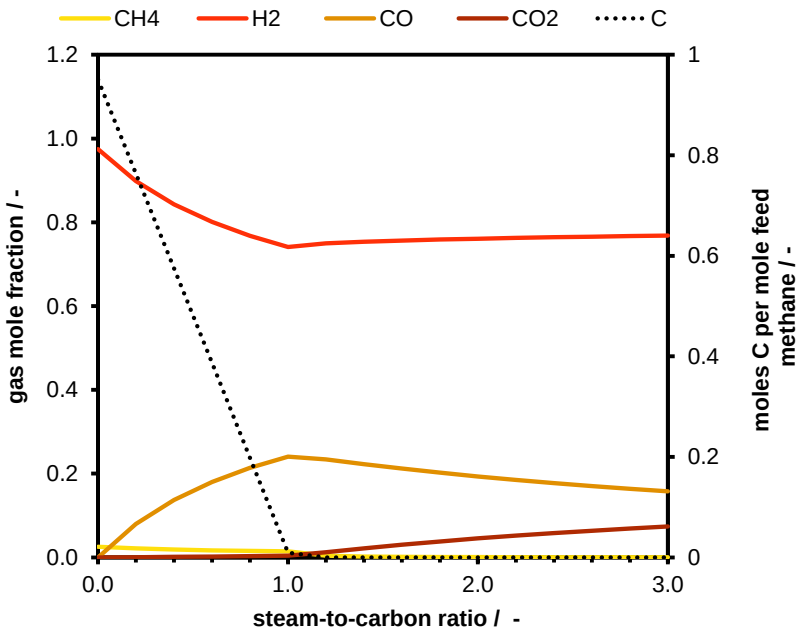

Figure 4.1.: Product gas molar composition of a methane steam reformer (MSR) as a function of the feed steam-to-carbon (S/C) ratio at 850 °C. The product is in chemical equilibrium and was calculated by Gibbs free energy minimisation. The water fraction was subtracted from the result.

Figure 4.1 shows the equilibrium composition as a function of the feed steam-to-carbon ratio (S/C) at a constant temperature of 850 °C. For presentational purposes the water fraction was subtracted out. It can be seen that the hydrogen content is above 0.6 in the whole S/C range. The amount of hydrogen is almost constant for S/C ratios above 1, whereas changes of CO and CO_2 can be noticed due to the occurence of the water-gas shift reaction. The high hydrogen content for small S/C values is explained by thermal decomposition of feed methane, as shown in equation (2.13). The main side product is carbon monoxide, which reaches a maximum fraction of 0.24 at a S/C ratio of 1 and is continuously reduced with increasing steam fraction in the feed. Obviously, at S/C = 1 only reaction (2.9) can occur, as only one mole water per mole methane is available for reaction. With increasing steam in the process, reaction (2.11) and water-gas shift reaction also take place, reducing the fraction of CO and producing CO_2. Small fractions of methane in the product are only present for very low S/C ratios.

A region of carbon formation was detected for S/C ratios below 1. Above this value, carbon-free operation can be guaranteed, when the chemical equilibrium is reached in an ideal operation. Below S/C = 1, carbon formation shows a linear trend. At S/C = 0, all methane is decomposed to hydrogen and solid carbon. With increasing S/C ratio dry decomposition and reaction (2.9) occur side by side. When enough water is present in the process at S/C = 1, the reforming reaction is favoured over thermal decomposition. It is concluded, that the

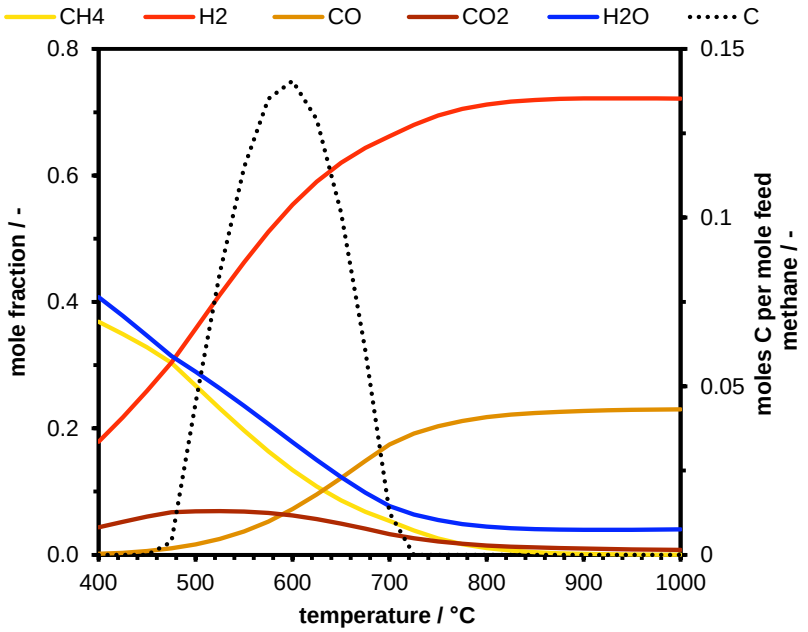

Figure 4.2.: Product gas molar composition of a methane steam reformer (MSR) as a function of the operation temperature (S/C = 1.2). The product is in chemical equilibrium and was calculated by Gibbs free energy minimisation.

reforming reactions utilising water are generally favoured over dry methane decomposition as long the water fraction is sufficiently large in the process. However, small contributions of methane thermal decomposition can occur in the process, leading to carbon depositions on the catalyst.

Furthermore, the equilibrium composition at a constant S/C ratio of 1.2 was determined as a function of the operating temperature, which is shown in figure 4.2. It was assumed that enough energy can be provided in order to guarantee isothermal operation conditions. A large range of hydrogen content variation was witnessed, with a steady hydrogen fraction above temperatures of 800 °C. At lower temperature levels, not all fuel is converted and part of the methane is still present in the product gas. At low temperatures, up until 500 °C, reforming hardly takes place. At the given feed compostion, the formation of CO is favoured over CO_2. This is indicative of reaction (2.9) being dominant, as not enough water is present for conversion of methane via reaction (2.11). For high temperatures, the WGSR equilibrium also favours the formation of CO over CO_2.

The results show a region of possible carbon formation between 460 °C and 720 °C. By regarding the reaction equilbria of the Boudouard reaction (figure 2.7), methane decomposition (figure 2.8) and reverse gasification (figure 2.9), it can be seen that all three reactions are likely to contribute to carbon formation in this range. However, methane decomposition

Table 4.1.: Summary of operating and boundary conditions and comparison of measured and calculated temperatures in the prototype simulation runs.

	Cycle 1	Cycle 3	Cycle 5	Unit
$\dot{m}_{in}$	0.79	1.36	1.41	$g/\,min$
S/C	2.64	2.43	2.11	-
T_w	807	855	857	°C
$T_{min,exp}$	726	735	732	°C
$T_{min,sim}$	734	710	689	°C
ΔT	8	-25	-42	°C

is more probable to have a significant effect in the upper part of this range, while carbon formation via the other two reactions is more likely to occur in the lower part. As high feed conversion is desirable, operation temperatures of 800 °C should be achieved, which also prevent carbon formation at the present S/C ratio.

4.2. Prototype

As illustrated in figure 4.3, the temperature in the prototype decreases rapidly at the beginning of the catalyst bed (z = 0.1 m), but is restored to inlet temperature long before the fluid reaches the outlet. However, the temperature is also reduced against the direction of the flow, which is a consequence of thermal conduction inside the porous bed as well as diffusion against flow direction as discussed in section 4.3. The flow direction can be read from the temperature profiles, as the lower temperature region is slightly stretched towards the reactor outlet. This effect is most significant in cycle 5, which uses the biggest mass flow, albeit of similar magnitude in all three simulation runs. In light of this trend it is expected that an increased amount of methane in the feed gas generally causes the lower-temperature region to expand towards the reactor outlet. Another important observation can be explained by the magnitude of energy, which is supplied to the reactor. Although the temperature difference in cycle 5 is much bigger than in cycle 1, the low-temperature regions have a very similar shape and spatial extent. This behaviour is attributed to the thermal boundary condition at the wall, where a constant temperature was set. Subsequently, a higher radial temperature gradient occurs and thus a greater driving force for thermal conduction according to Fourier's law, which causes a higher heat flux at the reactor wall adjacent to the region of reduced temperature.

Table 4.1 summarises the main results from the three prototype simulations, which were

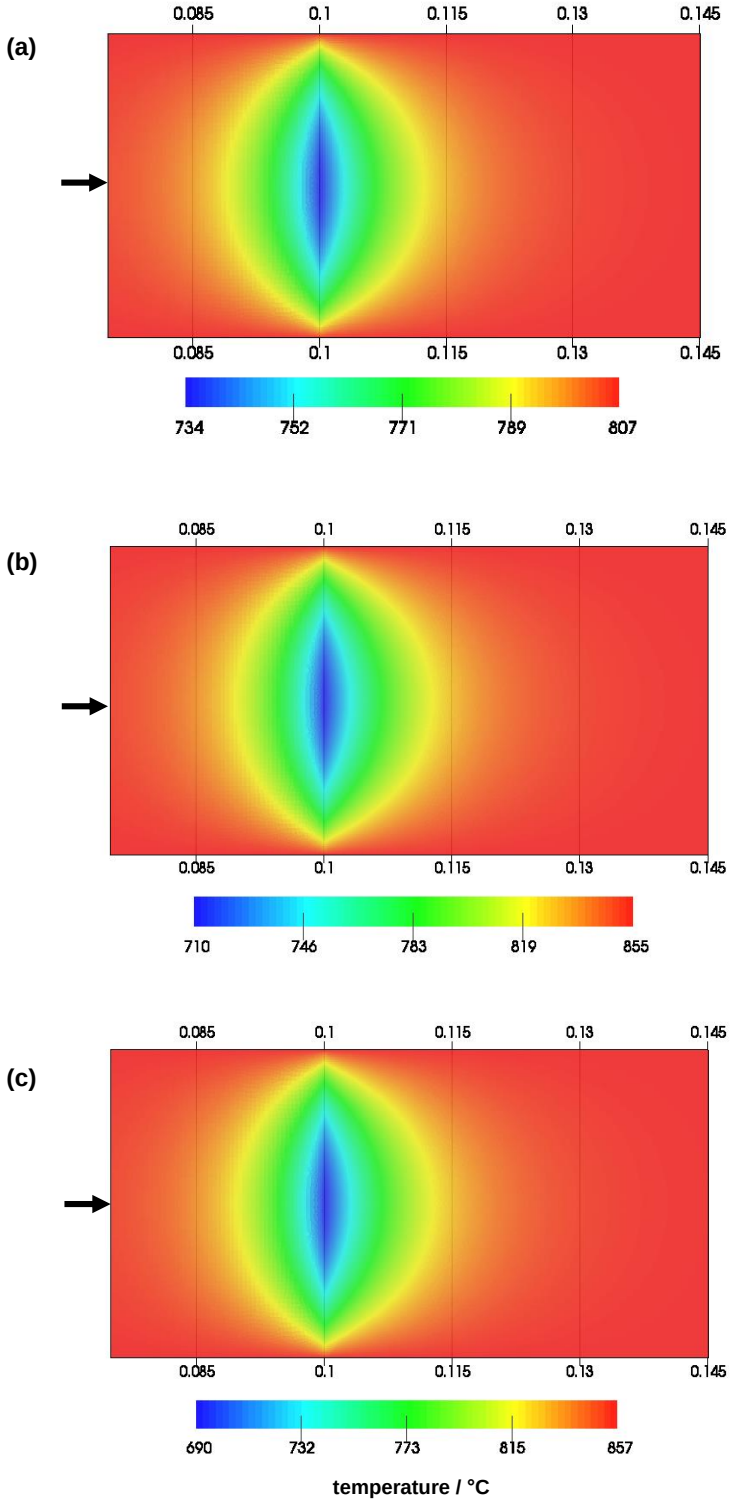

Figure 4.3.: Temperature (°C) in the prototype reactor calculated for simulation runs cycle 1 (a), cycle 3 (b) and cycle 5 (c) with flow directions from left to right. For illustrative purposes only the middle section of the reactor is shown. Beginning of the catalyst bed at z = 0.1 m.

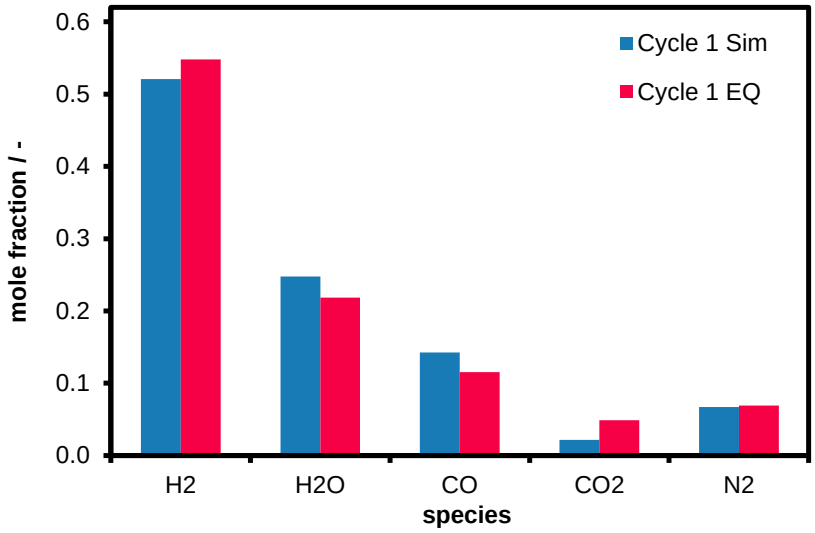

Figure 4.4.: Comparison of outlet molar composition of the CFD simulation and equilibrium composition for prototype cycle 1, T = 807 °C.

conducted in order to compare the theoretical model with the results of the experiments by Nestl [11]. It can be seen that for cycle 1 the calculated temperature correlates with the measured value, whereas the deviation for cycle 3 and 5 is bigger. As mentioned before, the low-temperature regions are of similar sizes in all three prototype simulations while the minimum temperatures are different. Thus, the reaction rates in cycle 5 are much higher than in cycle 1, which leads to a more rapid consumption of energy by the reforming reactions and a subsequent larger temperature drop between inlet and beginning of the catalyst bed. On the other hand, full methane conversion was achieved both in prototype experiments and simulations. This supports the hypothesis that the maximum possible reaction rates on the catalyst in the laboratory experiments are limited and are lower than the model suggests. If so, practical conversion must be slower than predicted by the simulation. If this is the case, the model also over-predicts the temperature drop.

As shown in figures 4.4 - 4.6, full methane conversion is achieved in all cycles. The fuel is mainly converted to hydrogen and carbon monoxide, while the carbon dioxide content is low. The ratio between carbon monoxide and carbon dioxide corresponds to the Boudouard equilibrium (figure 2.7), as at high temperatures carbon monoxide is more likely to exist. The increased nitrogen content during cycle 1 is explained by the higher inlet concentration, as visible in table 3.6. In all simulation runs, the CO fraction is higher than the equilibrium composition at the given wall temperature, while CO_2 shares are lower. The same trend was detected for the hydrogen fraction, which is lower than the equilibrium suggests and the water fraction, which is higher. That being said, the reason behind this trend is the water-gas shift reaction not being executed until the equilibrium in the simulation, but settling down on

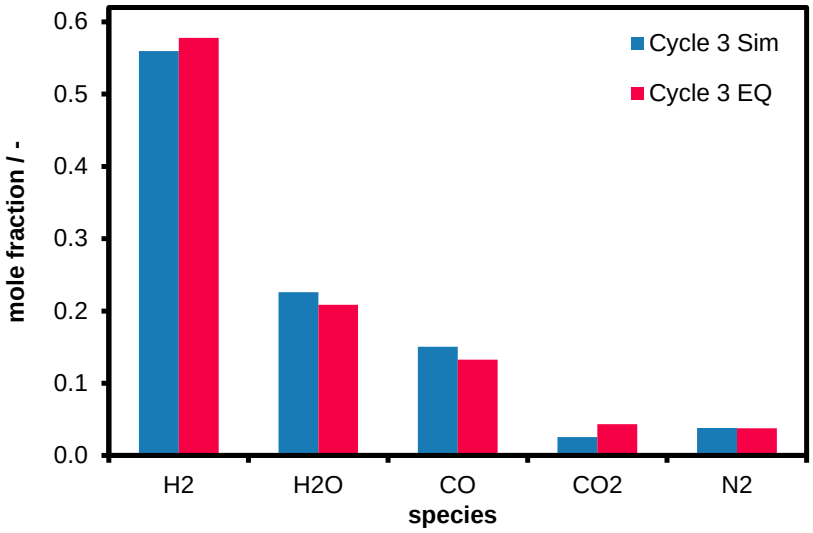

Figure 4.5.: Comparison of outlet molar composition of the CFD simulation and equilibrium composition for prototype cycle 3, T = 855 °C.

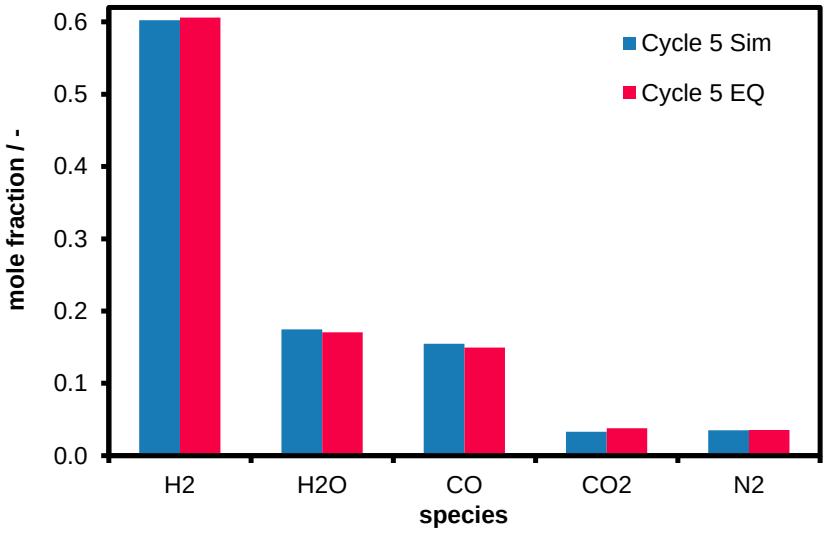

Figure 4.6.: Comparison of outlet molar composition of the CFD simulation and equilibrium composition for prototype cycle 5, T = 857 °C.

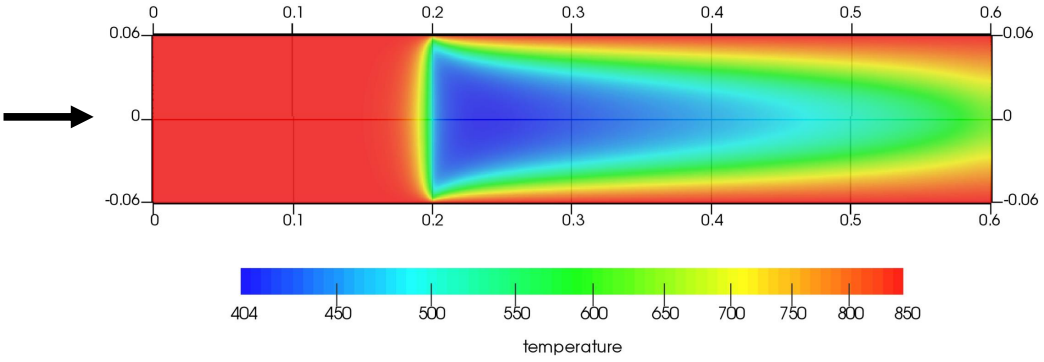

Figure 4.7.: Temperature (°C) in the industrial-scale diameter reactor, flow direction from left to right. Beginning of the catalyst bed at z = 0.2 m.

the left side of reaction (2.10). The corresponding equilibrium compositions were calculated by Gibbs energy minimisation at the inlet temperature of the respective simulation run.

With full conversion in mind, the temperature deviations between experiments and calculations are suspected to be caused by kinetic limitations of the catalyst, which are not represented in the reaction rate model. Reasons for the over-estimation of reaction rates are suspected to stem from both reaction rate and diffusional limitations of the catalyst. These properties slow down the MSR reactions and subsequently stretch the reactive zone along the axis. Thus, while the practical occuring temperature drop is smaller, the cold zone is also lengthened and full methane conversion is reached further down the reactor. As the abovementioned characteristic features of the catalyst are not yet known, it was assumed that the model reflected the laboratory process correctly, but describes the performance of an ideal catalyst without the inhibition by kinetic limitations. Having said this, the reaction rate achieved in the simulation exceeds possible experimental values. Therefore, all further interpretation must take this limitation into account and include it in all drawn conclusions.

4.3. Reactor

Figure 4.7 shows the calculated temperature distribution for the d_l = 120 mm reactor. A significant decrease of temperature was observed at the beginning of the catalyst bed at z = 0.2 m due to the onset of the endothermic MSR reactions. As seen in the prototype simulations, energy transport against flow direction takes place, which already leads to values below feed temperature in the non-reactive porous section. This temperature decrease is suspected to be caused by thermal conduction and mass transport against the direction of

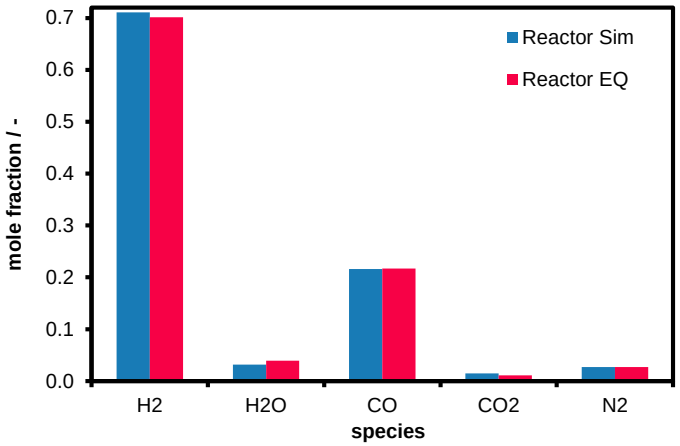

Figure 4.8.: Comparison of outlet molar composition of the CFD simulation and equilibrium composition for the large reactor, T = 850 °C.

the flow. Figure 4.9 shows an elevated hydrogen fraction before the start of the active bed. The volumetric expansion due to the reforming reactions combined with diffusion against flow direction are the reasons for this effect. Towards the outlet the temperature increases continuously, as heat is supplied at the wall and transported through the reactor. A minimum temperature of 404 °C was observed, located in the first layers of the catalyst bed at the centre line. At the reactor outlet, the temperature varies radially between the prespecified wall temperature of 850 °C and a minimum value of 620 °C at the symmetric axis.

Due to the pseudo-homgeneous nature of the model approach, almost no radial mixing occurs in the front section of the reactor. This is evident from figure 4.10, which describes the radial velocity component inside the reactor. However, as reactions start the fluid comes into motion towards the reactor centre due to the increase of volume in reactions (2.9) and (2.11). The sudden volume growth leads to an increase of local pressure and subsequently to a compensation of pressure differences by expansion. Thus, it is concluded that the maximum reaction rates occur in the points of maximum radial velocity, at z = 0.2 m close to the wall, as volume growth is also at its maximum value. Towards the reactor outlet, the radial velocity component points towards the reactor walls, which can be attributed to the same effect of volume increase in the reforming reactions.

Full methane conversion was achieved in the simulation, which results in the outlet composition presented in figure 4.8. Again, more CO than CO_2 is produced, with a higher relative share of CO in comparison to the prototype results. This is attributed to the steam-to-carbon ratio of 1.2, whereas the ratio ranges from 2.1 to 2.6 in the prototype calculations. As less water is present in the process, reaction (2.9) is favoured over reaction (2.11) and therefore the conversion to CO fostered. Furthermore, this supposition is supported by the fractions

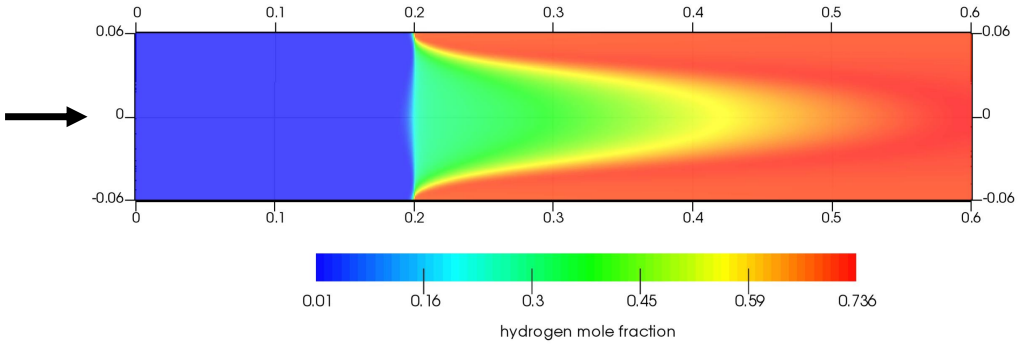

Figure 4.9.: Hydrogen mole fraction in the industrial-scale diameter reactor, flow direction from left to right. Beginning of the catalyst bed at z = 0.2 m.

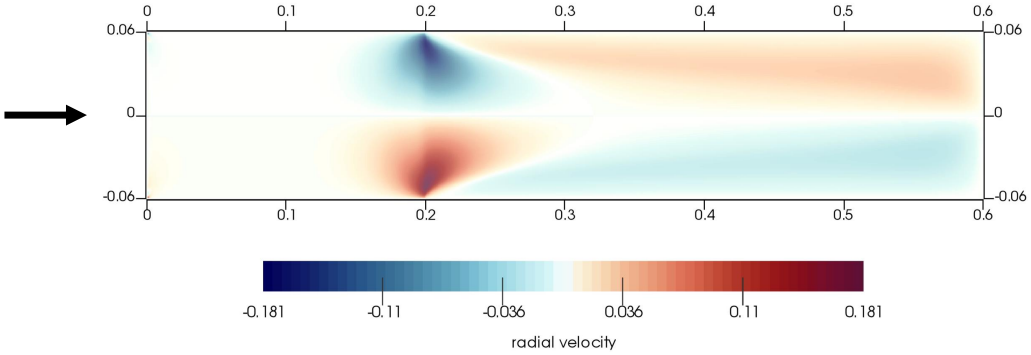

Figure 4.10.: Radial velocity field ($m \cdot s^{-1}$) in the industrial-scale diameter reactor, flow direction from left to right. Beginning of the catalyst bed at z = 0.2 m.

of water, which can be found in the product gas in the prototype simulations but not in the reactor off-gas. This also explains why the fraction of hydrogen in the reactor product is higher than in the prototype calculations. The calculated outlet composition correlates with the equilibrium composition. Thus, it is concluded that the syngas leaving the reactor has reached chemical equilibrium.

Figure 4.9 illustrates the calculated hydrogen mole fraction inside the reactor. Big radial differences in hydrogen conversion can be seen. Close to the reactor wall all present methane reacts instantaneously to hydrogen and the final hydrogen fraction is reached after only a few particle layers. In the centre of the reactor, reactions occur much slower. While some hydrogen is generated in the first few particle layers the reactions then seem to decelerate. Thus, a bell curve-shaped region of almost constant hydrogen mole fraction, visible in green color in figure 4.9 is formed. The reason for these radial differences is the radial variation of the local temperature. Endothermic reactions are promoted by high temperatures and therefore occur preferably in the vicinity of the wall, where the temperature is much higher than in the centre of the reactor. Towards the reactor outlet, however, the

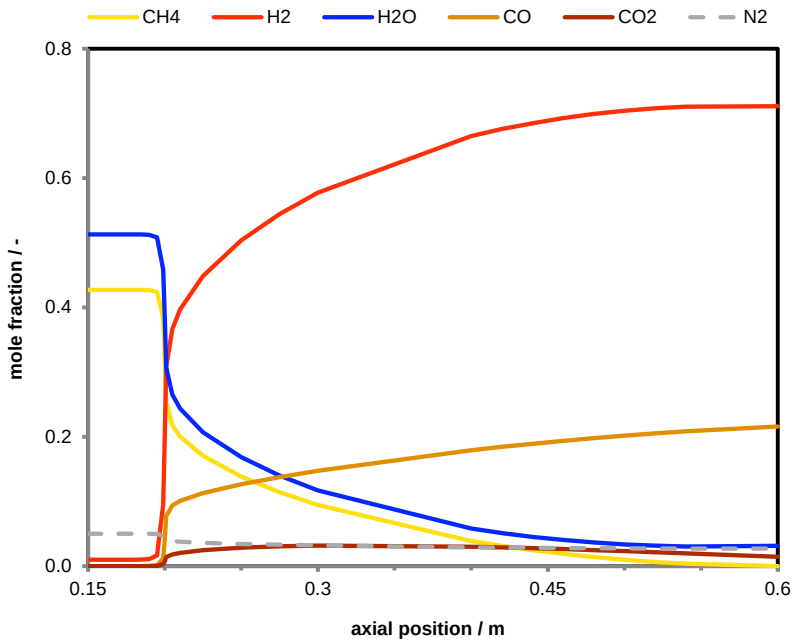

Figure 4.11.: Radial mass average molar composition in the reactor. Beginning of the catalyst bed at z = 0.2 m.

hydrogen fraction at the reactor centre increases until the outlet fraction is reached.

The radial mass averaged local composition is shown in figure 4.11. It can be observed that half of the feed gas is converted instantly when entering the catalyst bed at z = 0.2 m. After that, reactions decelerate and molar fractions change more slowly. Throughout the reactor, all methane is converted by the reforming reactions. However, after high reaction rates in the front section of the catalyst bed, small shares of methane are still present in most of the reactor. Another important thing to note is that the reforming process seems to start slightly before the start of the catalyst bed. However, this is an elusive observation, as the front section of the reactor is inert to reforming reactions. Instead, this phenomenon is explained by the diffusion of produced hydrogen against the direction of the flow. This is confirmed by the increased hydrogen fraction before the beginning of the catalyst bed, which can be observed in figure 4.9. In addition to local hydrogen contents in the last inert particle layers, enthalpy transport against flow direction also occurs when hydrogen diffuses towards the inlet. This means, that the lower temperature in the inert section discussed in figures 4.3 and 4.7 is not only caused by thermal conduction, but also by diffusive enthalpy transport against flow direction.

On account of the energy demand of the reactions and the constant wall temperature, a driving force for radial heat transport emerges. Figure 4.12 presents the heat flux through the reactor wall and the respective local temperature at the symmetric axis. The heat flux is directly representative for the size of the driving force according to Fourier's law, if the

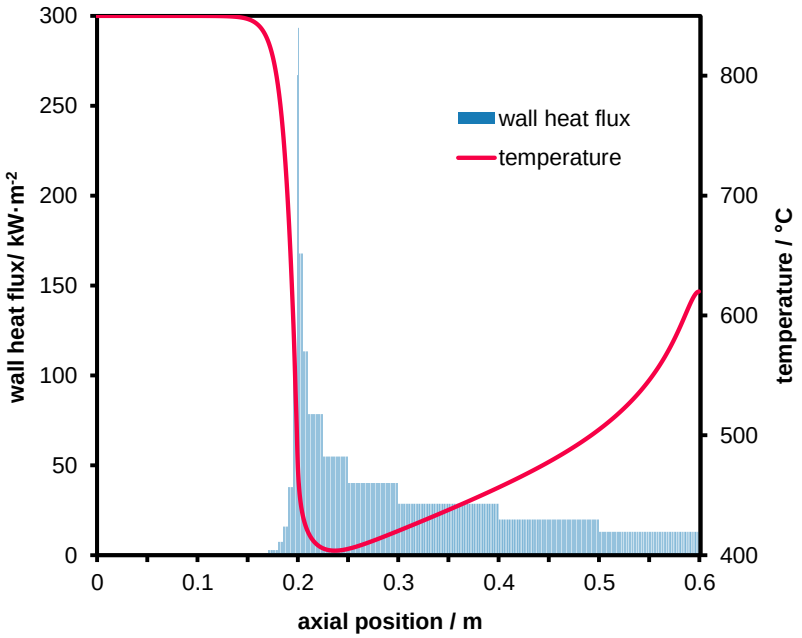

Figure 4.12.: Temperature at the centre line (r = 0, °C) and heat flux supplied at the inner wall ($kW \cdot m^{-2}$). Beginning of the catalyst bed at z = 0.2 m.

variation of the coefficient of thermal conductivity at the wall is considered small. Thus, the heat flux in the inlet section of the reactor is zero, as the temperature of the feed gas is equal to the wall temperature. Just before the start of the catalyst bed, a significant of heat demand can be observed. It corresponds with the lower-temperature region against flow direction previously discussed and detected in figure 4.7 and referred to in the discussion of figure 4.11.

At the starting point of conversion, the supplied heat flux reaches a global maximum at nearly 300 $kW \cdot m^{-2}$. This would, for example, lead to a heat demand of 2,26 kW for a tube wall segment of 20 mm. Thus, the heat demand in the first few particle layers of the catalyst bed exceeds possible practical values. As a consequence, the constant temperature boundary condition at the wall must be evaluated and refined in future studies.

As the energy is not transported to the centre of the reactor instantaneously, the temperature of the catalyst bed decreases. Down the reactor, heat is continuously brought into the system, which leads to a steady increase of the axial temperature towards the outlet. The heat flux is not directly proportional to the minimum temperature at the rotational axis. While the lowest temperature on the axis occurs at an axial position of z = 0.24 m, the maximum heat flux is demanded at the start of the catalyst bed az z = 0.2 m. In figure 4.7 it is visible that the high-temperature region at the reactor inner wall expands with increasing axial coordinate. The width of this region determines the driving force for thermal conduction at the wall and

thus the size of the wall heat flux.

After z = 0.24 m, the heat transported to the centre of the reactor exceeds the energy consumed by the reactions, hence the temperature starts to increase again. This happens, as reaction rates decrease due to low local temperatures as well as lower methane and water and higher product concentrations, which reduce the driving force for the reactions. This balance continuously shifts towards lower reaction rates and higher contribution of thermal conduction in the energy balance towards the reactor outlet, which is why the reactor temperature increases again.

Due to the low operating temperature at the beginning of the catalyst bed, carbon formation during the operation of the system must be expected. When the equilibrium composition (figure 4.2) is regarded, coke deposition is likely to happen in all parts of the catalyst bed, except in the regions close to the reactor wall. In the rear part of the reactor close to the wall, the main source of coking is expected to be the Boudouard reaction, as methane decomposition is unlikely due to the lack of methane, which was previously converted to hydrogen. Thus, carbon formation in parts with no methane present is mainly promoted by low temperatures.

A remedy for carbon formation can be provided by using a smaller feed flow or by raising the temperature at the wall, if the material can endure higher thermal stresses. Additionally, a higher steam-to-carbon ratio can lower the carbon formation temperature, but will also alter the synthesis gas composition by increasing the fraction of water in the product gas. Finally, if these measures are either not sufficient or realisable, alternative reactor design options must be evaluated. In order to facilitate heat transport towards the centre of the reactor, a smaller reactor diameter can be used. Moreover, a different heating strategy, such as internal heating, can be adapted in order to limit the temperature drop in the catalyst bed.

5. Conclusion

A mathematical model of a methane steam reformer was developed and implemented into a state of the art computational fluid dynamics (CFD) code. The model equations were formulated and solved for two different reactor types: a prototype reactor of 36 mm diameter, which was already tested experimentally and a large reactor of 120 mm diameter, which is currently built up. The results for the prototype reactor were used for a model validation purpose and are referred to in the discussion of the large reactor simulation results. The entire model development process is explained in detail in this work in order to enable further refinement of the model through future research activities in the field. Theoretical aspects relevant for the interpretation of the results were laid down in brief at the beginning of this thesis in order to define the scope of this work within the field of research.

The goal of this work was to evaluate a simple design option for the reforming section of a Reformer Steam Iron Cycle (RESC) application. Desired features of the fixed-bed reactor are a limited decrease of the operating temperature inside the catalyst bed in order to avoid carbon formation and full conversion of the supplied feedstock. The length of the reforming section is limited, as the rear part of the system must house the oxygen carrier, which is utilised for the subsequent production of pure hydrogen. By investigating the calculated temperature distribution inside the reactor the probability of carbon depositions on the catalyst surface was estimated.

The model was validated against previous measurements of a prototype reactor. While the comparison of experimental and computational results correlates, improbably high reaction rates are indicated. It is concluded that the model describes the reforming process on an ideal catalyst, which leads to an over-estimation of maximum reaction rates. Therefore, it is suggested that the reaction rate model must be adapted to the used material in order to returnl reaction rate values corresponding with the kinetic limitation properties of the given catalyst.

Results of the industrial-scale diameter reactor simulation suggest the presence of a low temperature region radiant from the centre and occupying a large amount of the reactor

volume. Due to the low temperature at the given steam-to-carbon ratio, large parts of the reactor show high affinity for equilibrium carbon formation. While the temperature increases towards the outlet, the product gas cannot be heated up to inlet temperature before leaving the reforming section. With the abovementioned reaction rate restriction in mind, it can be assumed that the reaction rate of the catalyst used in a bench-scale experiment would be lower than the calculated value, therefore leading to a smaller temperature drop in the reactor. However, if this was the case, methane conversion would decrease too and not reach 100% until the reactor outlet.

Due to strong variations of the heating demand along the reactor wall, a maximum heat flux at the beginning of the catalyst bed occurs. Further research must be conducted in order to investigate the validity of the constant wall temperature boundary condition set in this model. Practical restrictions during experiments will arise when the demanded heat flux cannot be provided to the reactor by the available heating system. This being said, the low-temperature region will be streched towards the outlet, when the required heating demand in the front section of the catalyst bed cannot be met.

Simulation results indicate that full methane conversion can be achieved by the large reformer. Moreover, carbon monoxide is the main by-product besides hydrogen. Equilibrium studies at the chosen operating point suggest S/C ratios above 1 and temperature of 800 °C or higher to avoid carbon formation in the process. A user-defined function, computing the reaction rates corresponding to a kinetic model from the literature, was implemented into the CFD code. The reaction rates compiled by the model are not yet validated against experimental results for the used catalyst material. In order to investigate feedstock conversion and, subsequently, discuss the magnitude of the temperature drop inside the catalyst bed, the material must be characterised. Furthermore, the maximum possible reaction rates for the used catalyst material must be determined and considered in the reaction rate model. The inclusion of so-called effectiveness factors in the kinetic model is seen as the most promising future model improvement.

One method to reduce the danger of coke formation on the catalyst is a re-evaluation of the operating point. Possible alterations of the operating conditions can lead to a lower probability of carbon formation. With the investigated reactor design, carbon formation can be reduced by increasing the wall temperature. A higher S/C ratio reduces the risk of coking but also influences the product gas composition. Alternatively, other design options for the reactor must be considered. As the temperature distribution is strongly dependent on the size of the reactor diameter, a thinner reactor is a promising option to deal with carbon formation. Moreover, a different heating strategy can be considered, in which heat is not

only supplied at the outer wall but for example also at the centre of the reactor by means of internal heating.

Several future model refinement opportunities were suggested. As mentioned before, firstly, an adaption of the reaction rate model to the results of an experimental catalyst characterisation by implementing effectiveness factors is seen as a promising improvement. Secondly, the customisation of the constant temperature wall boundary condition by comparing it to an exisiting heating device, allowing only a maximum local heat flux, is regarded as a valuable further development. Finally, the implementation of a thermal radiation submodel can provide further precision.

Overall, a detailed representation of a methane steam reforming reactor was developed. The model can be used for future studies and its modular approach enables the implementation of further submodels as well as the alteration of operating conditions.

List of Figures

List of Tables

List of Tables

Bibliography

[1] S. Dunn, “Hydrogen futures: toward a sustanable energy system,” *Int. J. Hydrogen Energy*, vol. 27, pp. 235–264, 2002.

[2] United Nations, “Adoption of the Paris Agreement,” United Nations Framework Conv. on Climate Change, Paris, Tech. Rep. December, 2015, pp. 1–32. [Online]. Available: `https://unfccc.int/resource/docs/2015/cop21/eng/l09r01.pdf%accessed:2016-08-09`.

[3] R. T. Watson *et al.*, “Greenhouse gases and aerosols,” International Panel on Climate Change (IPCC), Cambridge, New York, Melbourne, Tech. Rep., 1990, p. 40. [Online]. Available: `http://www.ipcc.ch/publications%7B%5C_%7Dand%7B%5C_%7Ddata/publications%7B%5C_%7Dipcc%7B%5C_%7Dfirst%7B%5C_%7Dassessment%7B%5C_%7D1990%7B%5C_%7Dwg1.shtml%accessed:2016-08-09`.

[4] International Enery Agency, “Key world energy,” Tech. Rep., 2014, p. 82. [Online]. Available: `http://www.iea.org/publications/freepublications/publication/key-world-energy-statistics.html%accessed:2016-08-09`.

[5] G. Voitic *et al.*, “High purity pressurised hydrogen production from syngas by the steam-iron process,” *RSC Advances*, vol. 6, no. 1, pp. 53 533–53 541, 2016.

[6] A. Messerschmitt, “Verfahren zur Erzeugung von Wasserstoff durch abwechselnde Oxydation und Reduktion von Eisen in von außen beheizten, in den Heizräumen angeordneten Zersetzern,” *DE 266863*, 1911.

[7] V. Hacker *et al.*, “Usage of biomass gas for fuel cells by the SIR process,” *J. of Power Sources*, vol. 71, no. 1-2, pp. 226–230, 1998.

[8] V. Hacker *et al.*, “Hydrogen production by steam-iron process,” *J. of Power Sources*, vol. 86, pp. 531–535, 2000.

[9] V. Hacker, “A novel process for stationary hydrogen production: The reformer sponge iron cycle (RESC),” *Journal of Power Sources*, vol. 118, no. 1-2, pp. 311–314, 2003.

[10] S. D. Fraser, M. Monsberger, and V. Hacker, “A thermodynamic analysis of the reformer sponge iron cycle,” *J. of Power Sources*, vol. 161, no. 1, pp. 420–431, 2006.

[11] S. Nestl *et al.*, “The production of pure pressurised hydrogen by the reformer-steam iron process in a fixed bed reactor system,” *J. of Power Sources*, vol. 280, pp. 57–65, 2015.

[12] J. R. Rostrup-Nielsen, “Production of synthesis gas,” *Catalysis Today*, vol. 18, no. 4, pp. 305–324, 1993.

[13] J. R. Rostrup-Nielsen, “Catalytic steam reforming,” in *Catalysis Sci. & Technology*, J. R. Anderson and M. Boudart, Eds., vol. 5, Springer, 1984, p. 130.

[14] D. Latham, “Mathematical modeling of an industrial steam reformer,” Master’s thesis, Queen’s University, Ontario, Canada, 2008, p. 256.

[15] A. L. Dicks, “Hydrogen generation from natural gas for the fuel cell systems of tomorrow,” *J. of Power Sources*, vol. 61, p. 113, 1996.

[16] O. Bey and G. Eigenberger, “Gas flow and heat transfer through catalyst filled tubes,” *Int. J. of Thermal Sci.*, vol. 40, no. 2, pp. 152–164, 2001.

[17] D. Trimm, “Coke formation and minimisation during steam reforming reactions,” *Catalysis Today*, vol. 37, no. 3, pp. 233–238, 1997.

[18] K. Hou and R. Hughes, “The kinetics of methane steam reforming over a Ni/alpha-Al2O catalyst,” *Chemical Eng. J.*, vol. 82, no. 1-3, pp. 311–328, 2001.

[19] J. M. Smith, “Interpretative review: heat transfer in fixed-bed reactors,” *Chemical Eng. J.*, vol. 5, pp. 109–116, 1973.

[20] E. L. G. Oliveira, C. A. Grande, and A. E. Rodrigues, “Steam methane reforming in a Ni/Al2O3 Catalyst: Kinetics and diffusional limitations in extrudates,” *Canadian J. of Chemical Eng.*, vol. 87, no. 6, pp. 945–956, 2009.

[21] J. Rostrup-Nielsen, “Sulfur passivated nickel catalysts for carbon-free steam reforming of methane,” *J. of Catalysis*, vol. 85, pp. 31–43, 1984.

[22] D. Trimm, “Catalysts for the control of coking during steam reforming,” *Catalysis Today*, vol. 49, no. 1-3, pp. 3–10, 1999.

[23] I. ANSYS, *Ansys Fluent Theory Guide*, 15.0, I. ANSYS, Ed., November. Canonsburg, PA: ANSYS Inc., USA, 2013, p. 780.

[24] B. Andersson *et al.*, “Turbulent flow modeling,” in *Computational Fluid Dynamics for Chemical Engineers*, 4th ed., Gothenburg, 2008, ch. 4, p. 217.

[25] A. G. Dixon and M. Nijemeisland, “CFD as a Design Tool for Fixed-Bed Reactors,” *Industrial & Engineering Chemistry Research*, vol. 40, no. 23, pp. 5246–5254, 2001.

[26] M. Nijemeisland and A. G. Dixon, “CFD Study of Fluid Flow and Wall Heat Transfer in a Fixed Bed of Spheres,” *AIChE J.*, vol. 50, no. 5, pp. 906–921, 2004.

[27] A. G. Dixon, M. Nijemeisland, and E. H. Stitt, “Packed tubular reactor modeling and catalyst design using computational fluid dynamics,” *Advances in Chemical Engineering*, vol. 31, pp. 307–389, 2006.

[28] A. G. Dixon, M. E. Taskin, M. Nijemeisland, and E. H. Stitt, “CFD method to couple three-dimensional transport and reaction inside catalyst particles to the fixed bed flow field,” *Ind. and Eng. Chemistry Research*, vol. 49, no. 19, pp. 9012–9025, 2010.

[29] Verein deutscher Ingenieure, *VDI-Wärmeatlas*, 11th ed. Düsseldorf: VDI-Gesellschaft Verfahrenstechnik und Chemieingenierwesen (GVC), 2013, p. 1784.

[30] P. Sadooghi and R. Rauch, “Experimental and modeling study of hydrogen production from catalytic steam reforming of methane mixture with hydrogen sulfide,” *Int. J. of Hydrogen Energy*, vol. 40, no. 33, pp. 10 418–10 426, 2015.

[31] I. ANSYS, *Ansys Fluent User’s Guide*, 15.0, A. Inc., Ed., November. Canonsburg, PA: ANSYS Inc., USA, 2013, p. 2620.

[32] S. Ergun, “Fluid flow through packed columns,” *Chemical Eng. Progress*, vol. 48, no. 2, pp. 89–94, 1952.

[33] B. E. Launder and D. B. Spalding, “Two-equation models of turbulence,” in *Lectures in mathematical models of tubulence*, 1st ed., London: Academic Press, 1972, ch. 5, p. 169.

[34] C. K. Harris *et al.*, “Computational fluid dynamics for chemical reactor engineering,” *Chemical Eng. Sci.*, vol. 51, no. 10, pp. 1569–1594, 1996.

[35] M. E. Taskin, A. G. Dixon, and E. H. Stitt, “Approximation of Reaction Heat Effects in Cylindrical Catalyst Particles with Internal Voids using CFD,” *Int. J. of Chemical Reactor Eng.*, vol. 5, pp. 1–15, 2007.

[36] J. G. Xu and G. F. Froment, “Methane steam reforming, methanation and water-gas shift .1. intrinsic kinetics,” *Aiche J.*, vol. 35, no. 1, pp. 88–96, 1989.

[37] M. Irani, A. Alizadehdakhel, A. N. Pour, N. Hoseini, and M. Adinehnia, “CFD modeling of hydrogen production using steam reforming of methane in monolith reactors: Surface or volume-base reaction model?” *Int. J. Hydrogen Energy*, vol. 36, no. 24, pp. 15 602–15 610, 2011.

[38] E. M. A. Mokheimer, M. Ibrar Hussain, S. Ahmed, M. A. Habib, and A. A. Al-Qutub, “On the modeling of steam methane reforming,” *J. of Energy Resources Technology*, vol. 137, no. 1, p. 012 001, 2014.

[39] L. Lao *et al.*, “CFD modeling and control of a steam methane reforming reactor,” *Chemical Eng. Sci.*, vol. 148, pp. 78–92, 2016.

[40] M. Gianotti Pret, D. Ferrero, A. Lanzini, and M. Santarelli, “Thermal design, modeling and validation of a steam-reforming reactor for fuel cell applications,” *Chemical Eng. Research and Design*, vol. 104, pp. 503–512, 2015.

[41] I. ANSYS, *Ansys Fluent UDF manual*, 15.0, I. ANSYS, Ed., November. Canonsburg, PA: ANSYS Inc., USA, 2011, p. 566.

[42] M. E. Taskin, A. G. Dixon, M. Nijemeisland, and E. Hugh Stitt, “CFD study of the influence of catalyst particle design on steam reforming reaction heat effects in narrow packed tubes,” *Ind. and Eng. Chemistry Research*, vol. 47, no. 16, pp. 5966–5975, 2008.

Appendix A.

Appendix

Table A.1.: List of indexes used in this work.

Index symbol	meaning
exp	value obtained in laboratory experiment
f	fluid quantity
i	species indicator
in	feed quantity
j	reaction indicator
min	minimum value
p	particle quantity
r	reaction quantity
sim	value obtained by numerical simulation
t	turbulent quantity
w	at the wall

Table A.2.: List of abbreviations used in this work.

Abbreviation	meaning
CFD	Computational Fluid Dynamics
DEN	Denominator
EWT	Enhanced Wall Treatment
FVM	Finite Volume Method
MIS	Mesh Independence Study
MSR	Methane Steam Reforming
PRESTO	Pressure Staggering Option
PSA	Pressure Swing Adsorption
RANS	Reynolds Averaged Navier-Stokes equations
RESC	Reformer Steam Iron Cycle
RNG	Renormalisation Group
SDK	System Development Kit
SIR	Steam-Iron Process
SOFC	Solid Oxide Fuel Cell
UDF	User-Defined Function
UF	Under-relaxation Factor
WGSR	Water-Gas Shift Reaction

Table A.3.: List of symbols used in this work.

Symbol	unit	meaning
A	varies	pre-exponential factor in Arrhenius equation
$C_{inertial}$	m^{-1}	inertial constant for pressure drop calculation
c_P	$J \cdot kg^{-1} \cdot K^{-1}$	specific heat coefficient
$C_{viscous}$	m^{-2}	viscous constant for pressure drop calculation
D	$m^2 \cdot s^{-1}$	diffusion coefficient
d_H	m	hydraulic diameter
d_I	mm	inner reactor diameter
d_p	mm	particle diameter
E	$J \cdot mol^{-1}$	activation energy
h	$J \cdot kg^{-1}$	specific enthalpy
H	J	total enthalpy
I	-	turbulence intensity
J	$kg \cdot s^{-1} \cdot m^{-2}$	diffusive mass flux
k	$J \cdot kg^{-1}$	turbulent kinetic energy
K_i	-	adsorption coefficient
k_j	varies	rate of reaction j
K_j	-	equilibrium constant
$\dot{m}$	$kg \cdot s^{-1}$	mass flow
N	-	tube-to-particle diameter ratio
p	Pa	pressure
ΔP	Pa	pressure drop
$\Delta P_{inertial}$	Pa	inertial share of pressure drop
$\Delta P_{viscous}$	Pa	viscous share of pressure drop
r	m	reactor radius
R	$J \cdot K^{-1} \cdot mol^{-1}$	ideal gas constant
S/C	-	steam-to-carbon ratio
S/V	-	surface-to-volume ratio
T	$^\circ C$	temperature

Table A.4.: List of symbols used in this work.

Symbol	unit	meaning
u_τ	$m \cdot s^{-1}$	friction velocity
U_∞	$m \cdot s^{-1}$	feed velocity from developed velocity profile
$\vec{v}$	$m \cdot s^{-1}$	velocity
y^+	-	dimensionsless wall distance
z	m	axial coordinate
ε	$J \cdot kg^{-1} \cdot s^{-1}$; -	dissipation rate of turbulent kinetic energy; bed porosity
λ	$W \cdot m^{-1} \cdot K^{-1}$	coefficient of thermal conductivity
μ	$Pa \cdot s$	dynamic viscosity
ρ	$kg \cdot m^{-3}$	density
$\overline{\overline{\tau}}$	Pa	stress tensor
τ_w	Pa	local wall shear stress

```
/*User-defined function used in the model of steam reforming*/
#include "udf.h"
DEFINE_VR_RATE(msr,c,t,r,mw,yi,rr,rr_t)
{
double y_co2=yi[4];
double y_n2=yi[5];
double y_co=yi[2];
double y_h2=yi[1];
double y_ch4=yi[0];
double y_h2o=yi[3];
double
Nsum,R,TP,temp,k1,k2,k3,Keq1,Keq2,Keq3,K_h2,K_co,K_h2o,K_ch4,DEN
,r1,r2,r3,dcb;

/*calculate species i in the unit of kgmol i/kg mix*/
y_co2 *= 1/mw[4];
y_n2 *= 1/mw[5];
y_co *= 1/mw[2];
y_h2 *= 1/mw[1];
y_ch4 *= 1/mw[0];
y_h2o *= 1/mw[3];

/*total mole number per kg mix */
Nsum = y_ch4 + y_h2o + y_h2 + y_co + y_co2 + y_n2;

/*calculate mole fraction of species i in the unit of kgmol
i/kgmol mix*/
y_ch4 *= 1/Nsum;
y_h2o *= 1/Nsum;
y_h2 *= 1/Nsum;
y_co *= 1/Nsum;
y_co2 *= 1/Nsum;
y_n2 *= 1/Nsum;

/*gas constant, J/molK */
R=8.314;

/*equilibrium constant calculated by the empirical formula*/
temp=C_T(c,t);
Keq1=10266.76*exp(-26.83/temp+30.11)*1e-4; /*bar^2, aus
Sadooghi, Rauch*/
Keq2=exp(4400/temp-4.063);
Keq3=Keq1*Keq2; /*bar^2*/

/*reaction rate constant*/
k1=4.225e+15*exp(-240100/(R*temp)); /*kmol*bar^-0.5*kg^-1*h^-1*/
k2=1.955e+6*exp(-67130/(R*temp));
k3=1.02e+15*exp(-243900/(R*temp));

/*adsorption coefficients*/
K_h2=6.12e-9*exp(82900/(R*temp));
K_co=8.23e-5*exp(70650/(R*temp));
```

```
K_h2o=1.77e+5*exp(-88680/(R*temp));
K_ch4=6.65e-4*exp(38280/(R*temp));

/*total pressure in the cell near wall, bar*/
TP=C_P(c,t)/(1.0e+5);

/*constant DEN factor for rate equations*/
DEN=1+TP*(K_ch4*y_ch4+K_co*y_co+K_h2*y_h2)+K_h2o*y_h2o/y_h2;

/*unit conversion to kmol/(m3.s) with density catalyst bulk*/
dcb=0.305556;

/*reaction rate equations*/
r1=dcb*k1/pow(TP*y_h2,2.5)*(pow(TP,2)*y_ch4*y_h2o-
pow(TP,4)*pow(y_h2,3)*y_co/Keq1)/pow(DEN,2);
r2=dcb*k2/(TP*y_h2)*(pow(TP,2)*y_co*y_h2o-
pow(TP,2)*y_h2*y_co2/Keq2)/pow(DEN,2);
r3=dcb*k3/pow(TP*y_h2,3.5)*(pow(TP,3)*y_ch4*pow(y_h2o,2)-
pow(TP,5)*pow(y_h2,4)*y_co2/Keq3)/pow(DEN,2);

if (!strcmp(r->name, "r1"))
{
*rr=r1;
}
else if (!strcmp(r->name, "r2"))
{
*rr=r2;
}
else if (!strcmp(r->name, "r3"))
{
*rr=r3;
}
else
{
Message("Unknown Reaction\n");
}
}
```

Table A.5.: Adopted values for water thermal conductivity ($W \cdot m^{-1} \cdot K^{-1}$) and dynamic viscosity ($Pa \cdot s$) for piecewise-linear approach [29].

Temperature / °C	λ	$\mu(10^5)$
350	0.04898	2.238
400	0.05465	2.245
450	0.06053	2.651
500	0.06659	2.856
550	0.07281	3.060
600	0.07917	3.261
650	0.08567	3.460
700	0.09228	3.657
750	0.09900	3.851
800	0.10580	4.043

Table A.6.: Polynomial constants for the specific heat capacity calculation via equation (A.1) [29].

	CH_4	H_2O	H_2
A	403.5847	1563.077	13602.45
B	9.057335	1.603755	3.402317
C	-0,01442509	-2.932784E-3	-3.358423E-03
D	1.580519E-05	3.216101E-06	-3.907953E-07
E	-6.343051E-09	-1.156827E-09	1.705345E-09

Table A.7.: Polynomial constants for the specific heat capactiy calculation via equation (A.1) [29].

	CO	CO_2	N_2
A	968.3898	429.9289	979.043
B	0.4487877	1.874473	0.4179639
C	-1.152217E-03	-1.966485E-03	-1-176279E-3
D	4.656882E-06	1.297251E-06	1.674394E-6
E	-7.34637E-10	-3.999956E-10	-7.256297E-10

Table A.8.: Polynomial constants for the thermal conductivity calculation via equation (A.2) [29].

	CH_4	H_2	CO	CO_2	N_2
A	0.009154	6.51E-04	-7.83E-04	-3.882E-03	-1.33E-04
B	8.11E-06	7.673E-04	1.0317E-04	5.283E-05	1.0149E-04
C	3.5153E-07	-6.8705E-07	-6.759E-08	7.146E-08	-6.065E-08
D	-3.3865E-10	5.0651E-10	3.945E-11	-7.031E-11	3.361E-11
E	1.4092E-13	-1.3854E-13	-9.47E-15	1.809E-14	-7.1E-15

Table A.9.: Polynomial constants for the dynamic viscosity calculation via equation (A.3) [29].

	CH_4	H_2	CO	CO_2	N_2
A	-7.759E-07	1.8024E-06	1.384E-07	-1.8024E-06	-1.02E-07
B	5.0484E-08	2.7174E-08	7.4306E-08	6.5989E-08	7.4785E-08
C	-4.3101E-11	-1.3395E-11	-6.2996E-11	-3.7108E-11	-5.9037E-11
D	3.118E-14	5.85E-15	3.948E-14	1.586E-14	3.23E-14
E	-9.81E-18	-1.04E-18	-1.032E-17	-3E-18	-6.7E-18

Table A.10.: Adopted values for catalyst specific heat capacity and thermal conductivity [29].

Temperature / °C	c_p / $J \cdot kg^{-1} \cdot K^{-1}$	λ/ $W \cdot m^{-1} \cdot K^{-1}$
400	989	4.78
600	1044	4.45
800	1080	4.30
1000	1107	5.00
1200	1133	6.05

Table A.11.: Mixture laws used for species mixing.

Property	approach
ρ	ideal gas
c_p	mixing law
λ	ideal gas mixing law
μ	ideal gas mixing law
mass diffusivity	kinetic theory

$$c_p = A + B \cdot T + C \cdot T^2 + D \cdot T^3 + E \cdot T^4 \tag{A.1}$$

$$\lambda = A + B \cdot T + C \cdot T^2 + D \cdot T^3 + E \cdot T^4 \tag{A.2}$$

$$\mu = A + B \cdot T + C \cdot T^2 + D \cdot T^3 + E \cdot T^4 \tag{A.3}$$

Model Setup in Ansys Fluent

- Setup
  - General
    - Pressure-Based Solver
    - Absolute Velocity Formulation
    - Steady Time
    - Axisymmetric 2D Space
    - no Gravity
  - Models
    - Energy – On
    - Viscous – RNG k-e, Enhanced Wall Fn
      - k-epsilon (2 eqn)
      - RNG
      - Enhanced Wall Treatment
    - Species – Species Transport, Reactions
      - Species Transport
      - Volumetric Reactions
      - Wall Surface Reactions
      - Heat of Surface Reactions
      - Aggressiveness Factor 0.5
      - Diffusion Energy Source on
      - Full Multicomponent Diffusion on
      - Mixture Material: „msrmixture"
      - Turbulence-Chemistry-Interaction: Finite-Rate/No TCI
  - Materials
    - Mixture: „msrmixture"
      - carbon-dioxide
      - nitrogen
      - carbon-monoxide
      - hydrogen
      - methane
      - water-vapor
      - Reaction: finite-rate
      - Mechanism: volumetric
    - Solid
      - alumina
  - Cell Zone Conditions
    - „prebed"
      - Material name „msrmixture"
      - Porous Zone on
      - Porous Zone
        - Direction-1 Vector: X: 1, Y: 0

        - Viscous Resistance
            - Direction-1 (1/m2) : 7.070609E+07
            - Direction-2 (1/m2): 7.070609E+07
        - Inertial Resistance
            - Direction-1 (1/m): 8965.078
            - Direction-2 (1/m): 8965.078
        - Heat Transfer Settings
            - Thermal Model: Equilibrium
            - Solid Material Name: "alumina"
    - „schalenkoerper"
        - Material name: "msrmixture"
        - Porous Zone on
        - Porous Zone as for "prebed"
        - Reaction on
            - Surface-to-Volume Ratio (1/m): 1889.764
            - Reaction Mechanism: mechanism-1
    - Porous Formulation: Physical Formulation
- Boundary Conditions
    - „axis-prebed"
        - axis
    - „axis-schalenkoerper"
        - axis
    - inlet
        - mass-flow-inlet
        - Mass Flow Rate specified
        - Turbulent Intensity specified
        - Hydraulic Diameter specified
        - Thermal
            - Total Temperature (k) specified
        - Species
            - Specify Species in Mole Fractions on
            - Species Mass Fractions specified
    - interface1
        - interior
    - interior-prebed
        - interior
    - interior-schalenkoerper
        - interior
    - outlet
        - pressure-outlet
        - Target Mass Flow Rate on and specified
        - Intensity and Hydraulic Diameter specified

                - Thermal
                    - Total Temperature (k) specified
                - Species
                    - Specify Species in Mole Fractions on
                    - Species Mass Fractions specified
            - schalenkoerper
                - interior
            - wall1
                - wall
                - Stationary Wall
                - No Slip
                - Thermal
                    - Thermal Conditions: Temperature
                    - Material Name: "alumina"
                    - Temperature specified
                    - Heat Generation Rate (W/m3): 0
            - wall2
                    - Thermal Conditions: Temperature
                    - Material Name: "alumina"
                    - Temperature specified
                    - Heat Generation Rate (W/m3): 0
    - Reference Values
        - Reference Zone: „prebed"
- Solution
    - Solution Methods
        - Pressure-Velocity Coupling Scheme: Coupled
        - Spatial Discretization
            - Gradient: Least Squares Cell Based
            - Pressure: PRESTO!
            - Density: Second Order Upwind
            - Momentum: Second Order Upwind
            - Turbulent Kinetic Energy: Second Order Upwind
            - Turbulent Dissipation Rate: Second Order Upwind
            - Species: Second Order Upwind
            - Energy: Second Order Upwind
        - Set All Species Discretizations Together: on
    - Solution Controls